UNIVERSITÀ DELLA CALABRIA

Dipartimento di Elettronica,
Informatica e Sistemistica

Dottorato di Ricerca in
Ingegneria dei Sistemi e Informatica
XXVciclo

Tesi di Dottorato

New Materials and Technologies for Compact Antennas and Circuits at Millimeter Frequencies

Antonio Borgia

DEIS- DIPARTIMENTO DI ELETTRONICA, INFORMATICA E SISTEMISTICA
Novembre

Settore Scientifico Disciplinare: ING-INF/02

UNIVERSITÀ DELLA CALABRIA

Dipartimento di Elettronica,
Informatica e Sistemistica

Dottorato di Ricerca in
Ingegneria dei Sistemi e Informatica
XXV ciclo

Tesi di Dottorato

New Materials and Technologies for Compact Antennas and Circuits at Millimeter Frequencies

Antonio Borgia

A Borgia

Coordinatore
Prof. Luigi Palopoli

Supervisore
Prof.ssa Sandra Costanzo

DEIS

DEIS- DIPARTIMENTO DI ELETTRONICA, INFORMATICA E SISTEMISTICA
Novembre

Settore Scientifico Disciplinare: ING-INF/02

to My Mother,
My Father
and My Sister

Acknowledgements

To Prof. Sandra Costanzo, supervisor of my PhD studies. I have achieved this goal thanks to her expertise and her help.

To Prof. Giuseppe Di Massa and the staff of Microwave Laboratory. I'm very pleased to have the chance of working in this qualified Group of Applied Electromagnetism.

To Mr. Ennio Marozzo, for his incoparable help and his matchless encouragement.

To my friends and my mates, for the gorgeous time we spent together.

To My Mother, My Father and My Sister, for everything they did, for everything they are doing and for everything they will do for me.

I met a lot of people during last years. Everybody have helped me to grow and left me something of important.

Thanks to everybody.

Antonio

Preface

The increasing demand for miniaturization of wireless systems has addressed strong interests in the development of new techniques for the realization of high–density millimeter–wave printed circuits.

The printed board size reduction, achievable at millimeter frequencies, fulfills well the compactness requirements of modern RF systems, however the high frequency behavior of standard dielectric substrates gives strong limitations to the performances and the feasibility of millimeter–wave printed components.

The dielectric materials, which usually show good electrical features in the lower microwave range, present high losses at millimeter frequencies. Research efforts are so devoted to the investigation of alternative materials and fabrication technologies for the realization of efficient low–loss radiating systems well working in the millimeter–wave range, but requiring minimal increase in cost.

In order to design printed circuits with good performances at high frequencies, the dielectric substrate should have low losses and a low dielectric constant, stable within the entire operating frequency range. As a consequence of this, the values of permittivity and dissipation factor, together with their thermal stability, should be considered for a proper material selection.

On the basis of the above considerations, the use of Benzocyclobutene (BCB) polymer as dielectric substrate for millimeter–wave printed structures is discussed in the first chapter of this PhD thesis. BCB is an organic material characterized by a stable relative dielectric constant and low losses over a broad millimeter frequency range. BCB has been successfully employed in literature as a covering film for packaging and interconnections on silicon substrates.

In the second chapter of the present PhD thesis, the adoption of BCB as low-loss dielectric substrate for the realization of compact circuits and antennas at millimeter-wave frequencies is proposed. Firstly, a specific technological process has been developed for the construction of single layer and multi-layer structures on BCB substrate. Then, an accurate experimental characterization

of BCB in terms of permittivity and loss tangent values has been performed within the range from 11 GHz to 65 GHz. These retrieved electromagnetic parameters have been subsequently adopted for the design of various kinds of millimeter-wave antennas. Finally, the realization and the experimental characterization of the synthesized prototypes have been performed and they are described in chapter 3.

In the last chapter of the thesis, micromachined millimeter wave antennas are presented. In particular, a new integrated platform is performed, in which the waveguide slot array is on the same substrate of the feeding microstrip line.

A specific synthesis procedure for the waveguide slot array is descibed and, in order to experimentally validate the design, a linear slot array prototype is fabricated and measured in the Microwave Laboratory at University of Calabria.

Contents

List of Figures

List of Tables

1

Emerging Materials and Technologies at Millimeter Frequencies

1.1 Introduction

In recent years, strong research efforts have been devoted to the investigation of innovative materials and fabrication technologies for the realization of efficient low–loss circuits and antennas well working at millimeter frequencies but requiring a minimal increase in cost.

To guarantee good performances as dielectric substrate at millimeter waves, the material should have low losses and a low dielectric constant, stable within the operating frequency range, so the values of material permittivity and dissipation factor should be accurately considered, but also the thermal stability of these parameters has a relevant role for a proper material selection, especially for space applications.

At millimeter wave frequencies, materials and integration techniques in RF system are subject to more performance constraints. One example in printed technologies is the substrate water absorption, which above 10 GHz can cause unacceptable losses in elements such as antennas, filters and trasmission lines, particulary over extended periods of time and under conditions of varying humidity.

Potential substrates with excellent performances extending throughout the millimeter–wave range can be found in the polymer category.

1.2 LTCC: Low–Temperature Co–fired Ceramics

LTCC is a ceramic multilayer technology composed from 2 to 100 layers with robust, hermetic and environmentally stable substrates. LTCC has a great potential for millimeter–wave applications, especially because of its low manufacturing cost, excellent performances and high level of integration.

The whole process for millimeter wave antenna and circuits needs a high accuracy and a small tolerance for implementation and it can be divided into seven steps [1].

Substrate Preparation: The unprocessed material for LTCC substrates must be preconditioned before the implementation due normally on a roll shipped with an applied foil which is used as a filling mask for the vias, and must be treated carefully, especially when the sheet is unrolled and cut, because arbitrary shapes of cavity and windows can be formed.

Via Forming: Vias may be punched or drilled with a low-power laser and normally filled with a conventional thick film screen or an extrusion via filler.

For blind vias is recommended to form the holes in the masks a bit smaller than their diameters.

Printing: The via printing process can have high resolution due to the flatness and solvent absorption properties of the tape.

Collating: Each layer is placed in turn over tooling pins. Some foundries use heat to fix the sheets one on the top of the other.

Lamination: Lamination can be done using two approaches. The first one named uniaxial lamination where the tapes are pressed between heated platens and the second one using an isostatic press where the stacked tapes are vacuum packaged in a foil and pressed in hot water.

Co-firing: The firing should be done under high temperature controlled as a function of time and varied according to the details of the process, but in one step on a smooth, flat setter tile.

Post-processing: Some materials need a post processing where the paste is to be applied after firing the tape and then a second firing is undergone

LTCC has some particular features, such as the availability of cavities where electronic components can be integrated for functional and environmental purposes. Because LTCC uses less metal and improves the robustness of the ceramic bonding, crosshatched ground planes can be done easily. LTCC can support three types of vias: RF shield , signal and thermal vias. The first one is used to isolate radiation coupling, the second one terminates in each layer in cover pads, and the third one is designed for thermal conduction where connecting planes are staggered with adjacent planes at each layer.

1.3 LCP: Liquid Crystal Polymer

A liquid crystal polymer (LCP) is an organic material identified as a thermoplastic polymer with unique structural and physical properties that offers a good combinations of electrical, thermal, mechanical and chemical properties.

LCPs gives a unique all-in-one solution for high–frequency designs due to their ability to act both as high–performance substrate and as packaging material for multilayer construction. In microwave design, it is attractive due to the low relative dielectric constants, low dissipation factors, and commercial availability of laminates.

Commercial LCP material is supplied in thin film with predefined thicknesses ranging and one side or both sides have a copper layer laminated in a vacuum press. LCP has a low cost, a lower water absorption that makes it relatively unaffected by moisture and humidity, and stable relative dielectric constant and loss tangent across a wide frequency range.

1.4 High–Temperature Superconducting

High–Temperature superconductor (HTS) are materials that behave as superconductors at unusually high temperatures. Normally, HTS are thin-film structures prepared by epitaxial growth on single crystal dielectric substrates.

HTS films have practical applications in modern microwave integrated circuits employed in aerospace applications and terrestrial mobile communication base stations, and offers the possibility of significantly reducing the weight and volume of the microwave equipment.

HTS epitaxial growth requires a process optimisation for film integrity with high level of expertise. Processing, materials, conditions and films properties all have to be controlled reliably for consistent films to be produced.

Suitable deposition methods for high-quality HTS films and proper substrate constitute the two major requirements for a real device. High dielectric constant means that components at high frequencies can be considerably smaller than in conventional circuits.

1.5 BCB: Benzocyclobutene

Among the several companies working on the development of new materials, the Dow Chemical Company[2] has recently developed a wide variety of polymers to be used as dielectric materials with low dielectric constant.

Since 80s, the Dow has proposed a very important family of polymers based on benzocyclobutene, better known as BCB. The BCB polymers have been widely adopted in microelectronic for the realization of packages and interconnections.

Only in 90s BCB has been also adopted for the realization of micro-chips, thus replacing the gallium arsenide (GaAs) in many applications. Furthermore, BCB has been adopted in flat panel displays and as covering resin for copper plates and printed circuits for telecommunication applications.

1.5.1 Principal Features of Polymeric Materials

A polymer is a macromolecule characterized by a high molecular weight, consisting of a large number of small simple units called monomers, that have a low atomic weight.

The polymeric materials can be classified according to their electrical conductivity. A first class of polymers is characterized by a high conductivity comparable to metals, a second group has conductivity values which are typical of semiconductors, and finally the most popular polymeric materials behave as insulators.

The physical/electrical properties of polymers are influenced by the following factors:

- *chemical composition*;
- *crystallinity degree*;
- *use of additives*;
- *molecular weight.*

The *chemical composition* fundamentally affects the material physical properties, such as the melting point and the processing temperature. On the contrary, the chemical constitution of the polymers has little influence on their electrical properties.

The relative permittivity of most commercial polymers varies between 2 and 3; the loss tangent, $\tan \delta$, can assume values ranging from $1 \cdot 10^{-4}$ up to $5 \cdot 10^{-4}$, for an operating frequency less than 1 GHz; the resistivity can vary between 109 Ωm and 1016 Ωm.

The *crystallinity degree* affects the polymer hardness. As matter of fact, for given chemical compositions and molecular weight, the polymeric materials having a greater crystallinity degree will have a higher hardness and, as a consequence, a higher softening temperature.

The *use of additives* has the purpose to improve some material features, such as the thermal stability, the electrical properties and the chemical resistance. For example, the addition of stabilizers allows to prevent the deterioration that many plastics suffer as a result of sunlight (UV rays), oxygen and heat.

The polymers *molecular weight* is the product of the molecular mass of the structural unit for the degree of polymerization. Usually a polymer has a molecular mass of at least 1000 units, or a degree of polymerization equal to 100.

1.5.2 General features of BCB

The hydrocarbon benzociclobutene can be realized through the pyrolysis[1] of the *α-cloro-o-xilene*. The treatment of the hydrocarbon with bromine

[1] Pyrolysis is a thermochemical decomposition of organic material at elevated temperatures without the participation of oxygen.

produces 4-bromo-BCB. The coupling of 4-bromo-BCB with the divinyltetramethylsiloxane, in the presence of palladium as a catalyst, produces the monomer DVS-bis-BCB (Fig. 1.1).

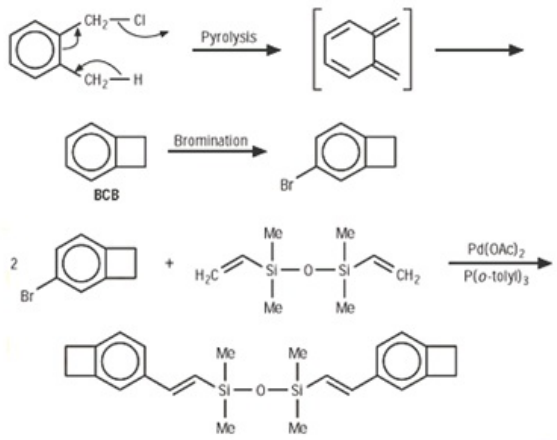

Fig. 1.1. Cyclotene realization process.

If necessary, the monomer can be distillated in order to reduce the presence of ionic impurities. The monomer can be realized in two steps. Once the curing reaction is started, it is purposely interrupted before the atomic bonding of every monomer molecules. The resulting oligomer can be completed in a second stage. The open-loop thermal reaction of the four terms of BCB produces o-quinodimethane. This intermediate product readily undergoes a Diels-Alder reaction with the available dienophiles[2].

On the contrary, in absence of dienophiles, the o-quinodimethane reacts with itself so giving the dimers 1,2,5,6-dibenzocyclooctadiene or undergoes a polymerization similar to that of the 1,3-diene giving the poly-xylene. The Diels-Alder reaction dominates in the B-phase of DVS-bis-BCB thus generating, in the next step, the final product.

In 1992 the Dow Chemical Company began to market the Cyclotene series 3022, which corresponds to the semi-treated solution of BCB. Following this first launch, in 1994, the Cyclotene series 4000 was proposed, which is a photosensitive polymer obtained by the use of the diazonium salt[3].

Cyclotene is a material very suitable for millimeter wave applications, whose characteristics can be summarized as follows:

[2] Hydrocarbon containing two double bonds.

[3] This salt when combined, in alkaline applications, with the azodye (dye derived from nitrobenzene), chemically reacts and changes color.

- Relative dielectric constant ε_r=2.65 (1 MHz - 10 GHz).

- Loss tangent tgδ=0.0008 0.002 (1 MHz 10 GHz).

- Breakdown voltage $V_{Bd} = 5.3 \pm 0.2 \cdot 10^6$V/cm.

- Leakage current during the dry etching:
▷ $4.4 \pm 0.5 \cdot 10^{-10}$ A/cm^2 (0.5 MV/cm);
▷ $6.8 \pm 0.8 \cdot 10^{-10}$ A/cm^2 (1.0 MV/cm).

- Leakage current during the photosensitization process:
▷ $2.9 \pm 1.4 \cdot 10^{-10}$ A/cm^2 (0.5 MV/cm);
▷ $4.7 \pm 1.6 \cdot 10^{-10}$ A/cm^2 (1.0 MV/cm).

- Volume resistance $1 \cdot 10^{19}$ Ω-cm.

- Density 1.05 g/cm^3.

- Crystallization temperature Tg: > 350°C.

- Tensile strength 87 MPa.

- Torsion resistance 2.9 GPa.

- Elongation resistance 8%.

- Processing shrinkage: < 5%.

- Negligible processing volatility.

- Processing kinetic:
1) Slow at low temperatures ranging from 210°C up to 250°C;
2) Fast at higher temperatures.

- Negligible migration of copper.

One of the most important features of Cyclotene is the small loss tangent value which assures very low losses. Furthermore the frequency behavior of both loss tangent as well as dielectric constant is almost constant up to a frequency of 1500GHz (see Fig. 1.2). This last feature, which has been never achieved with other materials, explains the reason why the Cyclotene is suitable for millimeter wave applications.

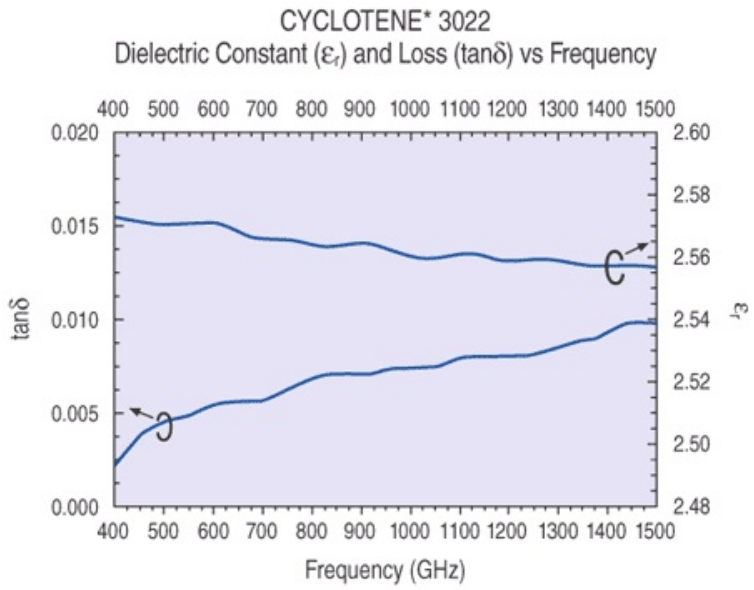

Fig. 1.2. Loss tangent and dielectric constant frequency behavior.

1.5.3 Cyclotene Series 3000

Cyclotene series 3000 is a resin derived from two bisbenzocyclobutene (BCB) monomers which tolerates dry etching process. This material has been developed for use as spin-on dielectric materials in microelectronic devices. The Cyclotene resins are low dielectric constant and low dielectric loss materials, furthermore they are characterized by the following features:

- low moisture absorption;
- no out-gassing;
- low temperature cure;
- excellent planarization.

The properties of Cyclotene 3000 are summarized in Fig. 1.3.

Property	Measured Value
Dielectric constant	2.65 – 2.50 at 1-20 GHz
Dissipation Factor	0.0008 – 0.002 at 1-20 GHz
Breakdown Voltage	5.3×10^6 V/cm
Leakage Current	6.8×10^{-10} A/cm2 at 1.0 MV/cm^2
Volume Resistivity	1×10^{19} Ω-cm
Thermal Conductivity	0.29 W/m°K @24°C
CTE	42 ppm/°C at RT
Tensile Strength	87 ± 7 MPa
Tensile Modulus	2.9 ± 0.2 GPa
Elongation	8 ± 2.5 %
Poisson's Ratio	0.34
Residual Stress	28 ± 2 MPa at RT
Tg	> 350°C
Moisture Absorption	< 0.2%

Fig. 1.3. Thermal, electrical and mechanical properties of Cyclotene series 3000.

1.5.4 Processing Procedure for Cyclotene Series 3000

The Cyclotene resins have been widely adopted in a variety of electronic applications. Usually they are used to realize very thin dielectric substrates for sandwich structures, characterized by a copper-dielectric-copper stratification. These structures can be obtained by adopting the dry etching process which is briefly described below.

The surface to be coated with Cyclotene resin should be free of inorganic particles and organic residues. The application of an adhesion promoter (AP3000) is recommended prior to BCB coating. The procedure for applying adhesion promoter on the substrate consists of the following steps:

- dispensing of the adhesion promoter;
- spreading through a spincoater with a speed ranging between 50 and 300 rpm (for 5 seconds);
- spin-drying at 2000-3000 rpm for 15-20 seconds.

Following the adhesion promoter process, BCB resin is spun onto the substrate. The coating process consists of the following steps:

1) Dispense of BCB resin: it can be done statically or dynamically (rotating the substrate at a speed of 50-200 rpm). In order to obtain good results, it is helpful to dispense the resin radially from the edge of the wafer to

the center. The dispense volume will depend on the thickness of the substrate. Usually, 2-3 ml of BCB are sufficient for a 15 cm^2 substrate surface.

2) Spreading through a spincoater with a speed ranging between 500 and 750 rpm (for 5-7 seconds).

3) Spin coating with a speed ranging from 1000 to 5000 rpm (for 20-30 seconds), which is appropriate to achieve the desired coating thickness reported in Fig. 1.4.

Spin Speed (RPM)	CYCLOTENE 3022-35	CYCLOTENE 3022-46	CYCLOTENE 3022-57	CYCLOTENE 3022-63
1000	2.26	5.46	13.8	26.2
1500	1.84	4.39	10.7	19.9
2000	1.59	3.76	9.04	16.5
2500	1.43	3.35	7.97	14.4
3000	1.30	3.05	7.21	12.9
3500	1.21	2.82	6.65	11.8
4000	1.13	2.63	6.20	10.9
4500	1.07	2.48	5.84	10.2
5000	1.01	2.35	5.55	9.64

Fig. 1.4. Thickness after cure (in microns) versus spin speed.

4) Removing the drops from the edges of the wafer, by decreasing the speed of the substrate up to 600-1000 rpm and distributing on the wafer rear side the T1100 solvent for 5-10 seconds. Finally the speed must be increased up to 1500 rpm for drying the back side of the wafer.

5) If necessary, the process can be repeated from step 1 to step 4 in order to increase the substrate thickness.

6) At the end of the process, the polymeric film should be properly treated in order to avoid the material deterioration during subsequent handling and curing operations. The drying treatment must take place in the absence of oxygen (<100ppm[4]). This last condition can be readily achieved by flowing inert gas (nitrogen or argon) through a convection oven, or by using a vacuum furnace or oven. This treatment should take place for about 4 - 5 hours, including the initial process of heating and the final of cooling. The drying process can be realized in two different ways which are defined as Soft-Cure (Table 1.1) and Hard-Cure (Table 1.2). The Soft-Cure process is applied when the wafer must be further processed, while the Hard-Cure returns the final product.

[4] ppm = parts per million.

Table 1.1. Soft-Cure.

Step #	Description
Step 1	5' up to 50°C
Step 2	15' up to 100°C
Step 3	15' up to 150°C
Step 4	60' up to 210°C
Step 5	Natural Cooling

Table 1.2. Hard-Cure.

Step #	Description
Step 1	5' up to 50°C
Step 2	15' up to 100°C
Step 3	15' up to 150°C
Step 4	60' up to 250°C
Step 5	Natural Cooling

Further details about the process are reported in [3] and [4].

2

Realization Technology of Millimeter-Wave Structures on BCB

2.1 Technology Description

The need to design and realize high frequency devices operating in the millimeter waves range has lead to the research of new materials able to offer good performances in terms of losses and fabrication accuracy.

In the Microwave Laboratory of the University of Calabria, the BCB polymeric material has been recently adopted as dielectric substrate for the realization of printed millimeter wave circuits. The use of this innovative material has required the development of a microtechnology based on two different processes named deposition and lithography.

The first one consists in the realization of the stratified structure, i.e. copper-dielectric-copper, through the deposition of both the BCB dielectric layer as well as the copper layer.

The second process is instead necessary for the printing of the circuit. The developed procedure has been successful applied to the realization of many millimeter wave printed circuits, showing a high degree of accuracy.

Furthermore, the proposed process is less expensive than the nanotechnology, usually adopted in the integrated electronics industry.

2.1.1 Photolitografy

Photolithography is a technique used in electronics for the construction of printed circuits. In this thesis work it has been used to print micrsostrip antennas, or more in general a microstrip circuits, onto a copper layer placed over a dielectric. The process involves several steps. A photoresist film is deposited onto the wafer where it will be printed the circuit (Fig. 2.1).

Fig. 2.1. Wafer.

Since the photoresist is a liquid, it must undergo a particular process of cooking in the oven in order to form a homogeneous and solid layer onto the whole surface to be treated. (Fig. 2.2).

Fig. 2.2. Photoresist film.

The wafer is covered with a mask representing the layout of the desired circuit and it is subsequently exposed to UV or laser rays. The photoresist, sensitive to light, changes its chemical-physical properties. There are two different types of photoresist, which are known as positive and negative photoresist. If a positive photoresist is used, the portion subjected to the light becomes more soluble in the developer solution and it is washed away. On the other hand, if a negative photoresist is used the unexposed portion is washed away (Fig. 2.3).

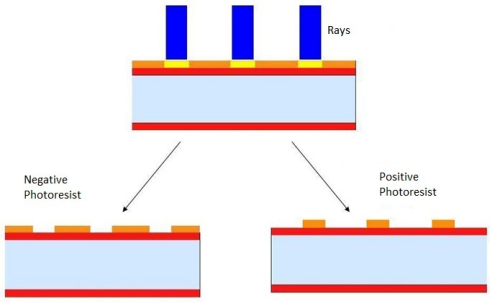

Fig. 2.3. Positive and negative photorerist after UV exposure.

The wafer is then immersed in a tank containing ferric chloride, capable of corroding the copper no longer protected by the photoresist film. The immersion time is closely related to the thickness of the copper. Usually, the ferric chloride corrodes also the walls of copper that are located under the photoresist. Due to this last undesired effect a greater portion of copper is removed (Fig. 2.4).

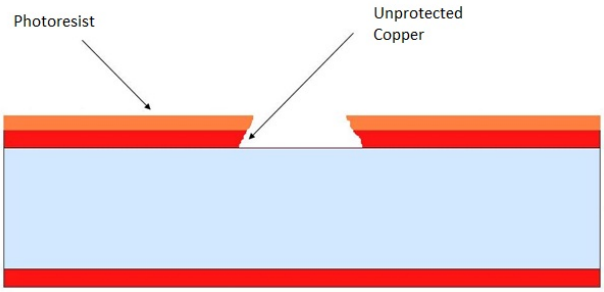

Fig. 2.4. UnderCut.

This effect, named *Undercut*, causes a decrease in the size of patch antennas and microstrip lines or, conversely, an increase in the size of slot lines. The undercut effect is closely dependent on the thickness of the copper. As matter of fact, when the thickness of the copper is greater the wafer must be dipped in ferric chloride for a longer time, then the undercut will be more relevant. This problem can be resolved by taking into account the undercut in the layout design.

In [5], it has been demonstrated that for copper plates with a thickness equal to 17 μm the undercut is equal to 35 μm, i.e. it is equal to twice the thickness. Since the most common laminates are characterized by a copper thickness ranging from 17 μm to 35 μm, the undercut may affect the accuracy

of printed circuits, especially in the millimeter frequency range where the size of the microstrip lines are comparable with the errors introduced by undercut.

Furthermore, it has been observed that the circuits printed with the photolithography process are usually characterized by irregular edges, as demonstrated by the microscope image illustrated in Fig. 2.5.

All these factors make the use of the described methodology inadequate for the realization of millimeter wave devices with the use of commercially available laminates.

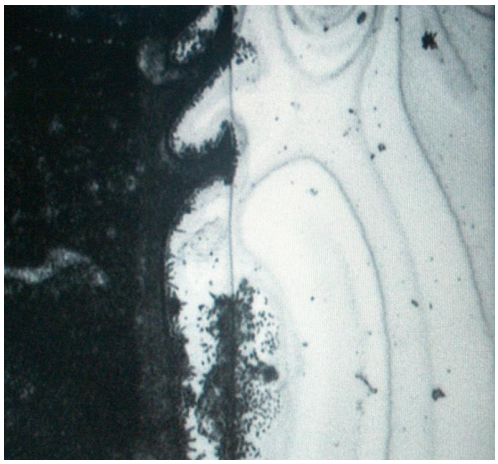

Fig. 2.5. Microscope image of a photolithography (17 μm copper laminate).

2.1.2 BCB and Copper Deposition

In order to realize a multilayer structure (copper-dielectric-copper) suitable for the fabrication of millimeter wave circuits, two different deposition techniques must be implemented.

The first one consists in the deposition of the polymeric material (e.g. Cyclotene) with a spin-coating process; the second one deals the copper deposition by evaporation.

The choice of using the spin-coating technique is imposed by the nature of the BCB material, while the evaporation technique is adopted to obtain the deposition of a very thin layer of copper, in order to reduce the undercut effect.

BCB Deposition

The Cyclotene series 3000 produced by Dow consists of four different resins, each characterized by a viscosity coefficient, which in turn affects the achievable film thickness (see table in Fig. 2.6).

Solution Properties	3022-35	3022-46	3022-57	3022-63
Solvent	Mesitylene	Mesitylene	Mesitylene	Mesitylene
Viscosity (cSt @ 25°C)	14	52	259	870
Thickness Range* (µm)	1.0 – 2.4	2.4 – 5.8	5.7 – 15.6	9.5 – 26.0

Fig. 2.6. Cyclotene viscosity coefficients.

These products allow to obtain dielectric layers with a thickness ranging from 1.0 μm up to 26.0 μm. In order to obtain thicker substrate layers, it is necessary to re-apply the spin-coating process.

The resin available at the Microwave Laboratory of the University of Calabria is the 3022-63. The Cyclotene processing steps reported under the Dow datasheets, and described in Paragraph. 1.5.4, have been properly modified in order to improve the effectiveness of the deposition process.

The experience has led to the definition of an optimal fabrication procedure, which is schematically illustrated by the block diagram in Fig. 2.7.

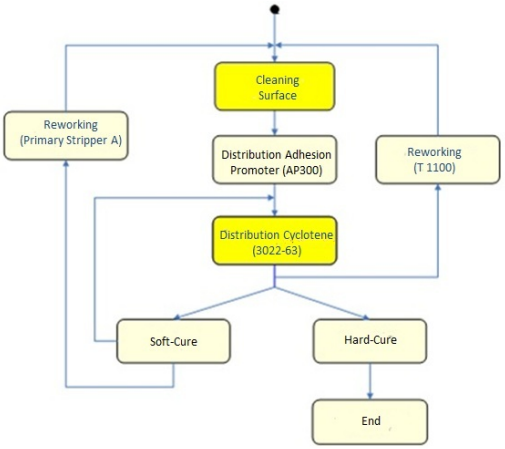

Fig. 2.7. Revised processing steps for Cyclotene series 3000.

In particular, the highlighted blocks show the critical steps which have required some adjustments. The implementation of this revised procedure has allowed to obtain higher realization accuracy.

A) Copper surface cleaning

The surface to be coated with Cyclotene resin should be free of inorganic particles, organic residues and other contaminants. Particles and residues cause coating defects and may lead to subsequent adhesion problems.

A brief treatment of O_2 plasma followed by a water rinse is usually sufficient for general cleaning purposes. However, in order to obtain better results, the following cleaning procedure has been adopted:

- the copper substrate is immersed in a solution of vinegar and salt for approximately one minute, in order to remove any presence of grease;
- the substrate is rinsed with de-ionized water, thereafter it is stored in a clean environment for the natural drying;
- the substrate is placed on the spin-coater and the vacuum pump is activated;
- the substrate surface is covered with the T1100 solvent in order to eliminate any additional surface residues, the spin-coater is programmed in order to execute the following actions:

1. acceleration from 0 *rpm* up to 1000 *rpm* in 1 *s*;
2. stasis at 1000 *rpm* for 10 *s*;
3. acceleration from 1000 *rpm* up to 2000 *rpm* in 1 *s*;
4. stasis at 2000 *rpm* for 10 *s*;
5. deceleration from 2000 *rpm* down to 0 *rpm* in 1 *s*;

the spin-coater is turned on until the programmed five steps are completed.

At the end of the described procedure the copper substrate is ready for the subsequent processing phases.

B) Cyclotene Dispensing

After the adhesion promoter process, described in paragraph and in Dow datasheets [3], [4] the Cyclotene 3022-63 is deposited onto the copper substrate. The desired thickness for the dielectric substrate is fixed to 26 μm. The Cyclotene dispensing process has been basically implemented as specified by Dow. However the process has been slightly revised, in order to obtain resin films with a higher degree of planarity and uniformity.

After removing the Cyclotene resin with the help of a pipette, the material is manually distributed in a radial manner from the center of the copper plate up to about one inch from the edge, as shown in Fig. 2.8. Usually, 2.4 *ml* of the resin are sufficient for a substrate with a surface area equal to about 50 cm^2.

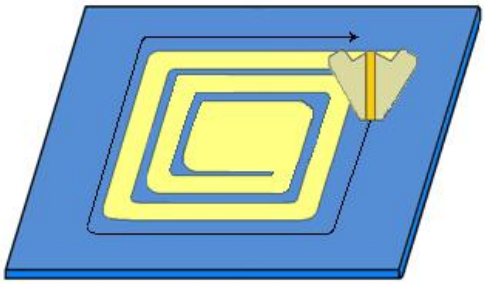

Fig. 2.8. Cyclotene dispensing process.

In order to obtain a high quality film layer, it is important to observe the following rules:

1. the pipette must never touch the substrate, in order to avoid the corruption of the adhesion promoter layer, that is interposed between the copper and the Cyclotene;
2. the resin must be distributed in a single shot.

Furthermore, if the resin is deposited too quickly, tiny air bubbles may be formed on the substrate surface. This phenomena must be avoided because during the Cyclotene polymerization process the air bubbles may explode, so leaving small craters on the substrate surface, as illustrated in Fig. 2.9.

During the copper deposition process, the metal fills the holes thus placing in conduction the deposited copper layer and the copper plate which is under the dielectric film.

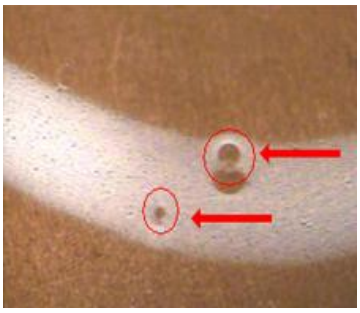

Fig. 2.9. Air bubbles on the Cyclotene film.

The observation of the previous rules assures the realization of a higher quality dielectric film. At this point, the coating procedure continues as described in *Copper Deposition*. A copper plate covered by a Cyclotene film, obtained at the end of the deposition process, is illustrated in Fig. 2.10. It

can be observed that the wafer is copper colored since the Cyclotene layer is transparent.

Fig. 2.10. Copper plate covered by a Cyclotene film.

Copper Deposition

As previously described, the deposition of a very thin layer of copper is indispensable for achieving very high resolutions with the use of a low cost lithographic technique. As matter of fact, the undercut effect is more relevant in the case of thicker copper layers.

In order to assure good resolutions in the realization of millimeter waves printed circuits, the thickness of the copper layer must be of the order of few μm.

There are only two techniques which allow to obtain these copper thickness values, namely the evaporation and the electroplating techniques. Both the processes can be implemented at the Microwave Laboratory of the University of Calabria through the use of a high-vacuum evaporator (Fig. 2.11) and a machine for the electroplating (Fig. 2.12).

Fig. 2.11. High-vacuum evaporator.

Fig. 2.12. Electroplating machine.

However, due to the desired high degree of planarization, the high-vacuum thermal evaporation technique is most adequate.

The deposition process consists of the following main steps [6]:

1. the components to be coated are placed in a chamber which is taken to a pressure up to $10 \cdot e^{-5}\ mBar$;
2. the materials that will constitute the coating are evaporated into the chamber;
3. the vapors, spreading inside the vacuum-room, reach the substrate where they condense;
4. the vapors condensation may occur in the presence of a gas, which is properly introduced into the chamber with the aim to obtain the deposition of a compound material.

The high-vacuum deposition techniques are ecological and allow to obtain high-purity films. Furthermore the vacuum avoids the the material oxidation.

The material evaporation (step 2) is realized by placing the copper into a container which is heated. The container must have a melting temperature higher than the copper evaporation temperature (1084.6°C). As a matter of fact, the copper is usually evaporated by using a tungsten (3422°C) or a tantalum (3017°C) container, which is heated through Joule effect (∼800A for a 12V voltage).

Fig. 2.13 shows a fabricated sample composed by 1m thick layer of copper deposited onto a Cyclotene film, which in turn is placed onto a copper plate.

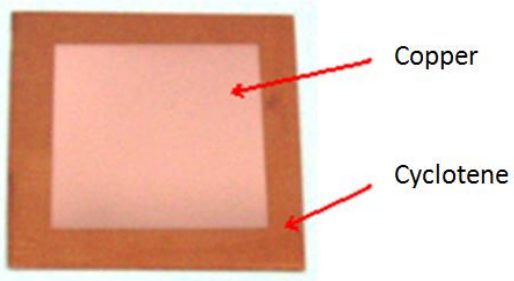

Fig. 2.13. Fabricated sample.

2.1.3 High Resolution Photolithography

The final step of the implemented fabrication procedure is the printing of the circuit onto the realized wafer.

The process consists of the following three steps:

1. layout definition;
2. photographic reproduction;
3. photo-development.

The circuit layout to be realized must be defined in a standard CAD file format, like DXF. The wafer surface is covered with the photoresist material through the spin-coater.

As test case a wafer composed by a layer of Cyclotene with a thickness equal to 26μm and a 1 μm thick layer of copper is considered. A Shipley Microposit S1813 SP-15 positive photoresist is dispensed onto the wafer surface, by adopting the spinning process described in Fig. 2.14.

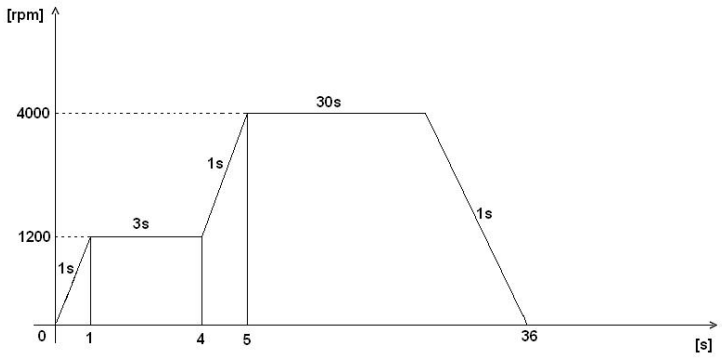

Fig. 2.14. Spinning process.

In order to dry the photoresist, the wafer is placed onto a plate at a temperature of 85°C for 30 minutes. The wafer is then submitted to laser exposure. In order to obtain a resolution of about 2 μm, the following settings are imposed to the laser machine: laser power equal to 20% and magnification equal to 20x.

The photo-development step consists of four phases:

1. development with the developer Shipley Microposit MF319 (into a dark room for 30-40s);
2. prototype stabilization through a thermal process on a hot plate at 105°C for 30 minutes;
3. chemical etching with a solution of ferric chloride (30%) and de-ionized water (70%) at a temperature of about 20°C;
4. photoresist removal through the Shipley Remover Microposit 1165.

The undercut due to the applied photolithographic process is of only 10 μm, with 4 μm due to the diffusion of the laser in the photoresist.

Furthermore, the circuits printed with the described technique are characterized by well defined boundaries with a scattering of less than 1 μm, as illustrated by Fig. 2.15.

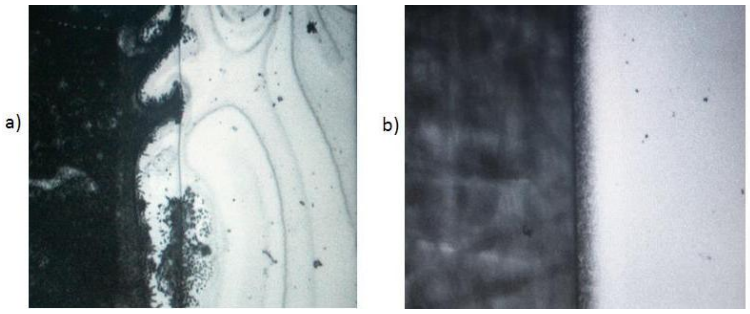

Fig. 2.15. Line printed with photolithography: **a)** 17 μm copper layer; **b)** 1 μm copper layer.

In conclusion the proposed microtechnology is suitable for the realization of millimeter wave devices such as antennas, filters, etc.

2.2 Dielectric Characterization of BCB at Millimeter Frequencies

The problem of accurate dielectric characterization of BCB is considered as a first task in order to guarantee the optimum design of microstrip lines and radiating structures.

Three papers in literature have investigated the basic electromagnetic properties of BCB. Results on BCB parameters in the frequency range from 1 GHz to 100 GHz are reported in [10] for single and multilayer microstrip lines of different cros-sections and lengths. An electro–optic characterization of thinfilm microstrip lines on Si substrate with polymerized cyclotene as dielectric between signal and ground conductor is performed in [11] to define the effective permittivity up to 100 GHz. In [12], the permittivity values of photosensitive BCB layers in the terahertz range are obtained from transmittance spectra measured with Fourier transform spectroscopy.

In this Section, a high frequency characterization of BCB permittivity is performed by using the polymer as dielectric material of conductor–backed coplanar waveguides (CBCPW). A schematic representation of the CBCPW prototype is depicted in Fig. 2.16, with the physical parameters described in Table 2.1.

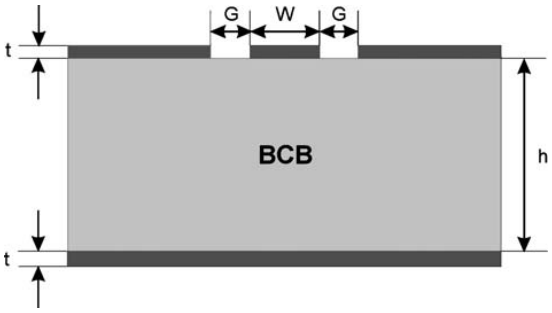

Fig. 2.16. Cross–section view of CBCPW prototype on BCB substrate material.

Table 2.1. Physical parameters of CBCPW prototype.

Parameter	Value	Specification
W	68.58μm	Central conductor width
G	30μm	Ground strip separation
t	1μm	Copper thickness
h	26μm	BCB substrate height
L	5.8mm	CBCPW length

The value of BCB thickness h is chosen equal to the maximum height for single coating (26 μm for the adopted Cyclotene series 3022 [12]) in order to simplify the realization process.

The central conductor width W and the ground strip separation G are chosen, by employing numerical simulations on commercial software Ansoft HFSS

[13], to match a 50 Ω characteristic impedance. The value of strip separation G is also limited by the 500 μm pitch probes subsequently used to perform measurements. All fabrication processes are performed into a Class 100 clean–room of Microwave Laboratory at University of Calabria, by following a three step procedure.

The BCB is firstly deposited on a copper ground plane having excellent planarity features, by using the spin coater type CaLCtec FR10 KPA, with a spin speed of 1000 RPM, in order to get the thickness of 26 μm. The resulting covered circuit is then cured in a convection oven under nitrogen at 250°C, to avoid polymer oxidation.

The top copper layer is then deposited by adopting the Physical Vapor Deposition (PVD) process based on thermal evaporation, and the circuit pattern is finally obtained by a lithography technique followed by wet–etch. A photograph of the CBCPW realized on BCB substrate through the technological process described above is reported in Fig. 2.17.

Fig. 2.17. Picture of CBCPW test prototype on BCB dielectric.

The probe–tip method [14] is adopted to extract the dielectric parameters of BCB from on–wafer S–parameter measurements. These are performed in the frequency range from 11 GHz to 65 GHz by using a vector network analyzer Anritsu 37397B and a probe station fitted with 500 μm GGB GSG contact probes. A photograph showing a particular of the connection between the CBCPW and the probe is reported in Fig. 2.18.

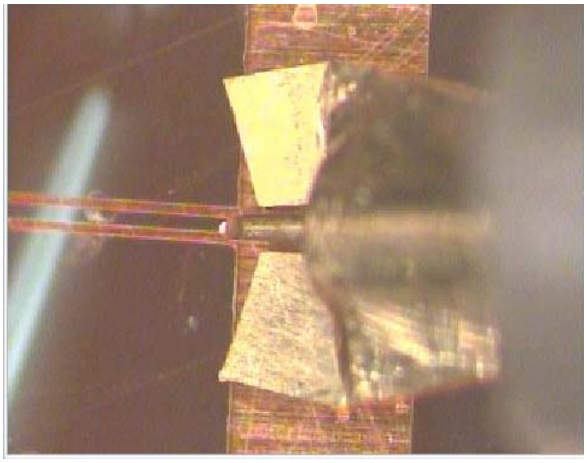

Fig. 2.18. Particular of the connection between the CBCPW and the probe.

A preliminary Line–Reflect–Reflect–Match calibration is applied, by using GGB Impedance Standard Substrate, to remove systematic error sources in the response of the test structure. However, non–calibrated measurement inaccuracies, primarily due to the non–ideal probe contact and positioning errors, are not eliminated. This is confirmed by the non–optimum behavior of the measured return loss in Fig. 2.19, assuming values above −10 dB within the frequency measurement range. In the same figure, the measured insertion loss of CBCPW on BCB substrate is also reported.

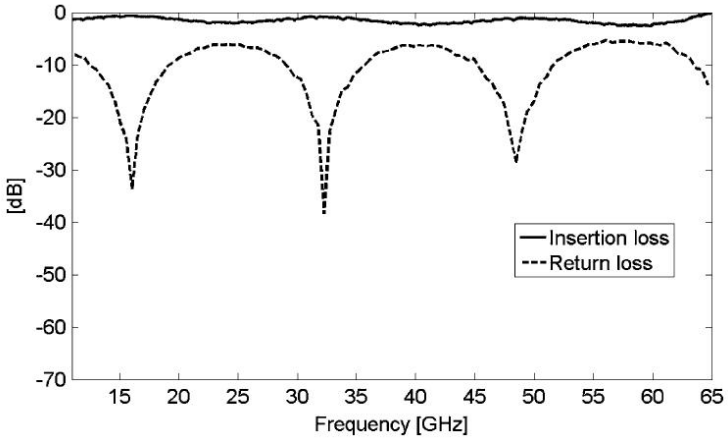

Fig. 2.19. Measured S–parameters of CBCPW on BCB substrate.

A quasi–TEM propagation mode is assumed on the CBCPW, which is modeled as an equivalent transmission line having characteristic impedance Z_C and complex propagation constant $\gamma = \alpha + \mathrm{j}\ \beta$.

Under ideal port–match conditions, the measured insertion loss properly describes the signal propagation $e^{-\gamma L}$ on the equivalent transmission line. However, the following generalized expression is adopted which relates the signal propagation $e^{-\gamma L}$ to the S–parameters of a lossy unmatched transmission line [15], in order to take into account the imperfect matching due to non–calibrated uncertainties:

$$e^{-\gamma L} = \left[\frac{1 - S_{11}^2 + S_{21}^2}{2S_{21}} \pm K\right]^{-1} \tag{2.1}$$

where:

$$K = \left\{\frac{(S_{11}^2 - S_{21}^2 + 1)^2 - (2S_{11}^2)}{(2S_{21})^2}\right\}^{\frac{1}{2}} \tag{2.2}$$

Measured S–parameters of CBCPW on BCB substrate are inserted into Eq. 2.1 to extract the attenuation and the phase constants α and β, respectively. The effective dielectric constant ε_{eff} is then computed from the phase constant β, whose plot is shown in Fig. 2.20, by using the relation:

$$\varepsilon_{eff} = \left(\frac{\beta}{k_0}\right)^2 \tag{2.3}$$

K_0 being the free–space propagation constant.

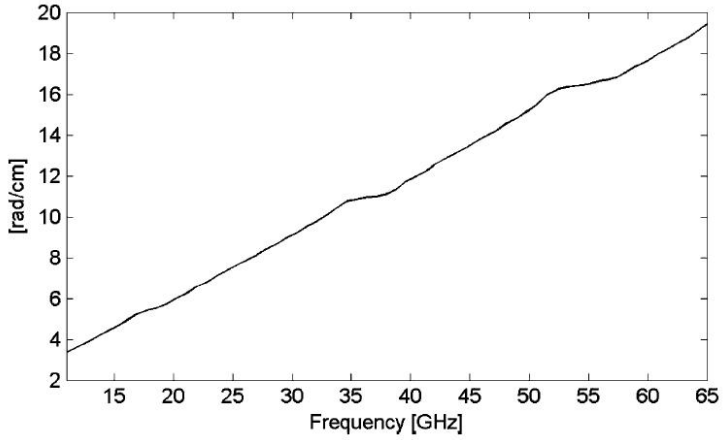

Fig. 2.20. Extracted phase constant β of CBCPW on BCB substrate.

The relative dielectric constant ε_r of BCB substrate material is finally obtained from ε_{eff} by using the analytical design expressions of CBCPW, based on a quasi–TEM approach and reported in [16]. An approximately steady value near the manufacturer specification $\varepsilon_{eff} = 2.65$ [12] is shown in Fig. 2.21, where a close agreement with the simulation results can be observed within the measurement frequency range.

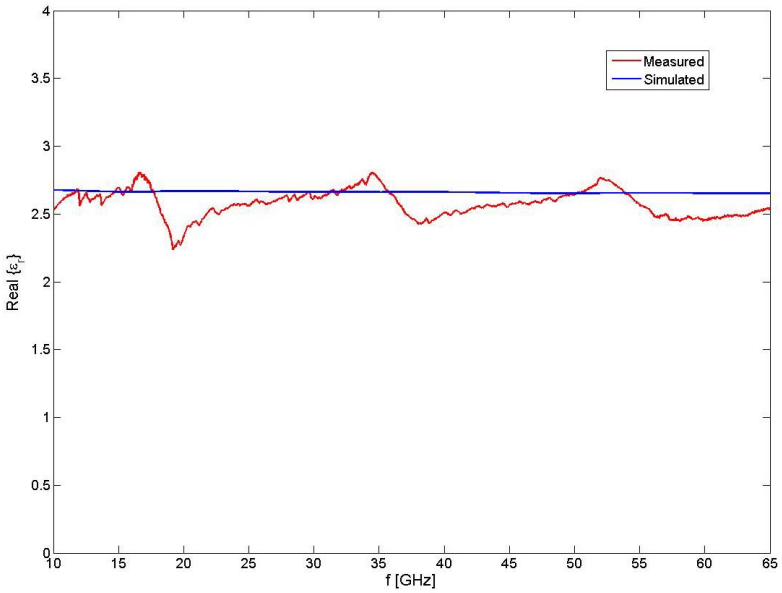

Fig. 2.21. Comparison between extracted (measured) and simulated dielectric constant ε_r of BCB substrate.

The extraction of BCB loss tangent has proven a more difficult task, as the attenuation constant α retrieved from Eq. 2.1 gives the total loss, including both conductor and dielectric contributions. In order to correctly retrieve the dielectric losses α_d due to BCB material, the subtraction of theoretical values for conductor losses α_c is performed from the total attenuation α by using the following model [17]:

$$\alpha_c = \frac{R'}{Z_C W} \cdot K_r \cdot K_i \tag{2.4}$$

where $R' = \sqrt{\rho \pi f \mu}$ is the skin resistance of conductor, ρ being the conductor resistance (ρ=1.78 $\mu\Omega$cm for Copper), f the operating frequency and μ the magnetic permeability. Parameter W into Eq. 2.4 gives the strip width and the terms:

$$K_r = 1 + \frac{2}{\pi} tan^{-1}\left[1.4\left(\frac{\Delta}{\delta}\right)^2\right] \tag{2.5}$$

$$K_i = e^{-1.2\left(\frac{Z_C}{Z_0}\right)^{0.7}} \tag{2.6}$$

represent, respectively, the correction factor due to surface roughness and the current distribution factor [17].

Parameters Z_C and Z_0 into Eqs. 2.4 and 2.6 give, respectively, the characteristic impedance of CBCPW, computed from the design expression in [16], and the wave impedance in vacuum. The term Δ is the rms deviation of surface roughness [17], here assumed equal to 0.05 mils, while δ is the skin depth.

The isolated dielectric attenuation is computed as:

$$\alpha_d = \alpha + \alpha_c \tag{2.7}$$

and the resulting values, illustrated in Fig. 2.22, are finally used to obtain the BCB loss tangent from the equation [18]:

$$tan\,\delta = \frac{\lambda_0}{\pi} \cdot \frac{\alpha_d \sqrt{\varepsilon_{eff}}}{\varepsilon_r} \cdot \frac{\varepsilon_r - 1}{\varepsilon_{eff} - 1} \tag{2.8}$$

λ_0 being the free-space wavelength.

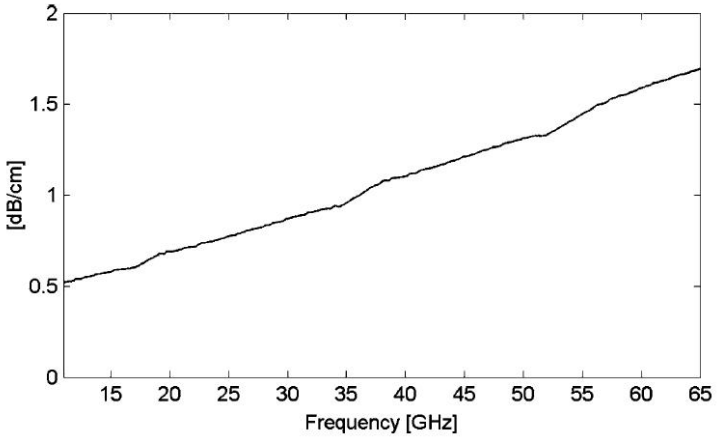

Fig. 2.22. Extracted attenuation constant α_d of CBCPW due to BCB dielectric substrate.

The extracted values of loss tangent, reported in Fig. 2.23, show a variation between 0.001 and 0.009 in the measurement frequency range from 11 GHz to 65 GHz. In the Literature, no similar experimental analysis has been

previously performed to characterize BCB losses, and the only reference data, agreeing with our measurement results, are those given by the producer [12]. The relatively low losses appearing in Fig. 2.23 make BCB a good candidate as substrate material for high–performance millimeter–wave planar structures.

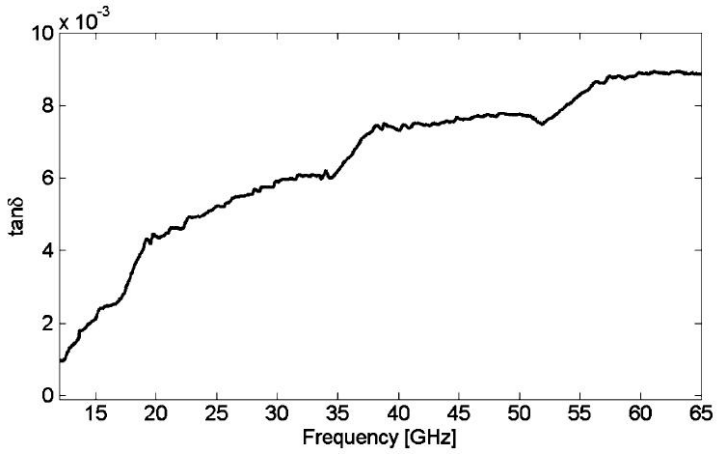

Fig. 2.23. Extracted loss tangent of BCB substrate.

2.3 Realization Examples

A first validation test of the manufacturing process for BCB-based microstrip structures has been performed on a CBCPW configuration. As a matter of fact, the coplanar structure is widely adopted at high frequencies in alternative to microstrip lines, because providing best features in terms of dispersion and radiation losses, and also for its easy fabrication and integration capability.

To simplify the realization process, the value of BCB thickness is chosen equal to the maximum height for single coating (26 μm for the adopted Cyclotene series 3022 [12]).

In this case, a hard-cure process is adopted which is typically carried out for realizing a single polymer layer, and leads to achieve 100% conversion from liquid to solid. The central conductor width W and the ground strip separation G are chosen by simulations on commercial Ansys software to match a 50 Ω characteristic impedance.

The values of loss tangent previously determined (Fig. 2.23) are used for the accurate characterization in the simulation stage. A photograph of the realized 7 mm length CBCPW on BCB substrate is reported in Fig. 2.24.

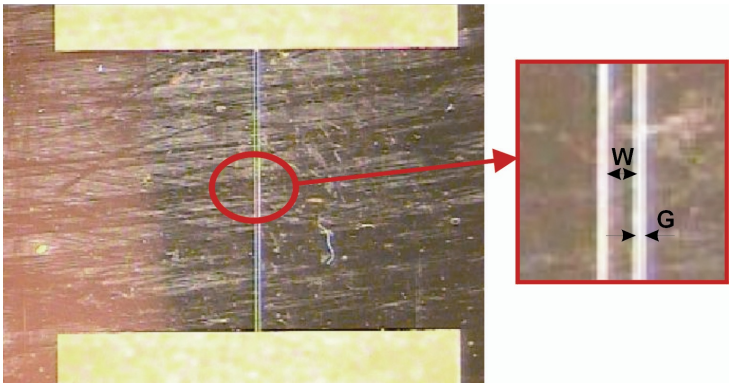

Fig. 2.24. Photograph of the realized CBCPW on BCB substrate (W=70μm, G=30μm).

The experimental validation of the CBCPW prototype is performed by using a vector network analyzer Anritsu 37397B and a probe station fitted with 500 μm GGB GSG contact probes (Fig. 2.25).

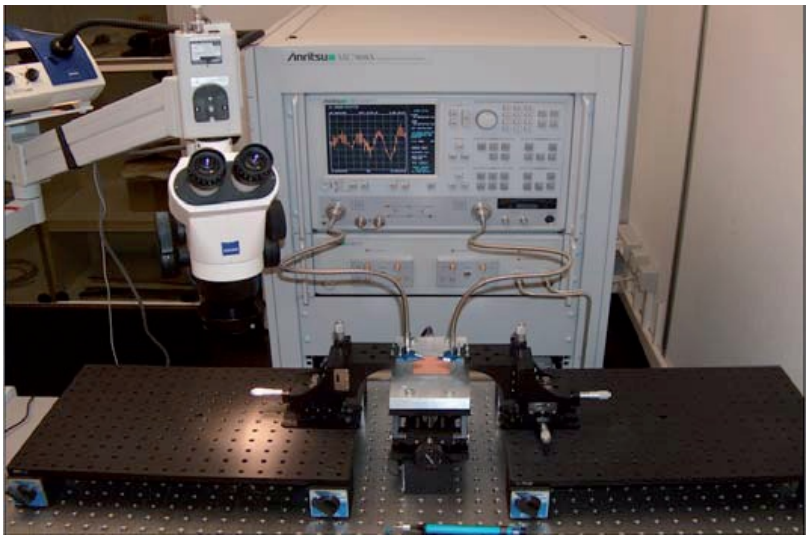

Fig. 2.25. Photograph of the test setup for the experimental validation of CBCPW on BCB substrate.

The comparison between measured and simulated CBCPW insertion loss is illustrated in Fig. 2.26. The non-perfect agreement between them can probably be attributed to some non-calibrated measurement inaccuracies, primarily given by the probe contact and the positioning errors.

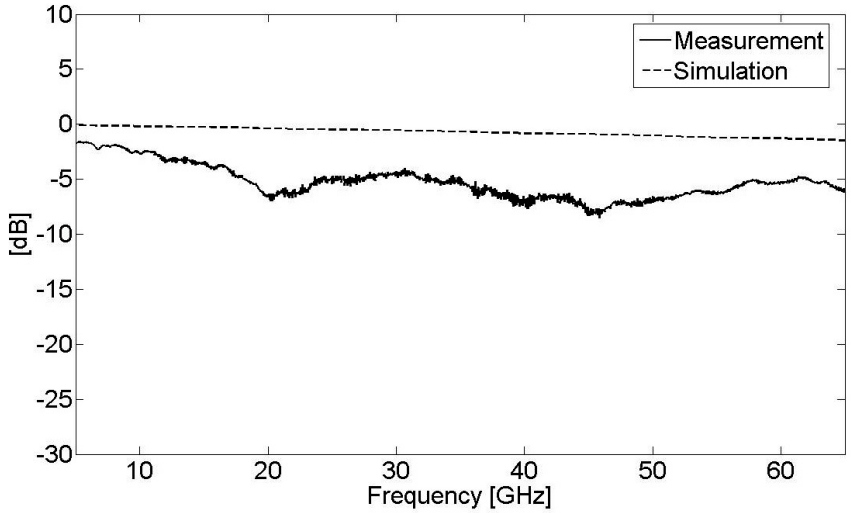

Fig. 2.26. Comparison between simulated and measured insertion loss of CBCPW on BCB substrate.

As a further validation example, a V-band inset patch antenna has been designed on a BCB dielectric substrate. The layout of the antenna prototype, with the full indication of all dimensions, is reported in Fig. 2.27.

In order to perform on-wafer measurements, a microstrip-to-coplanar waveguide transition is also included in the design, as illustrated in Fig. 2.27. The patch antenna is realized on a single layer of BCB, having thickness equal to 26 μm.

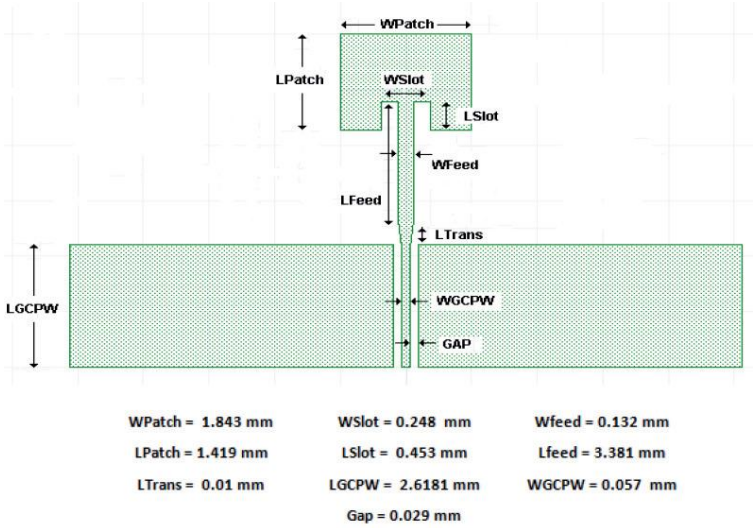

Fig. 2.27. Layout and dimensions of V-band patch antenna on BCB substrate.

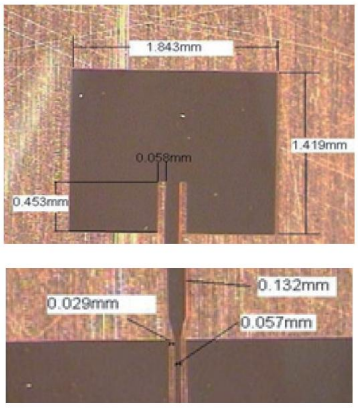

(a)

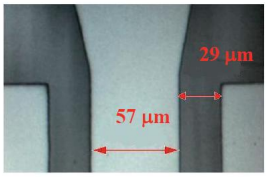

(b)

Fig. 2.28. (a) Photograph of the realized V-band patch antenna and (b) particular of the microstrip-to-coplanar waveguide.

The simulation characterization is performed by assuming the exact loss tangent at the design frequency as reported in Fig. 2.23, approximately equal to 0.009. In the realization stage, a 0.5 mm copper layer is first adopted as deposition support for the BCB dielectric layer. A hard-cure process is then applied to realize the BCB polymerization and a 1 μm copper layer is subsequently deposited by the vaporization procedure.

The antenna layout is finally etched by a laserwriter machine. A photograph of the realized V-band antenna prototype, with a particular showing the microstrip-to-coplanar waveguide transition, is reported in Fig. 2.28.

The test setup adopted to perform on-wafer measurements is illustrated in Fig. 2.29, and the excellent comparison between the simulated and the measured return loss is reported in Fig. 2.30.

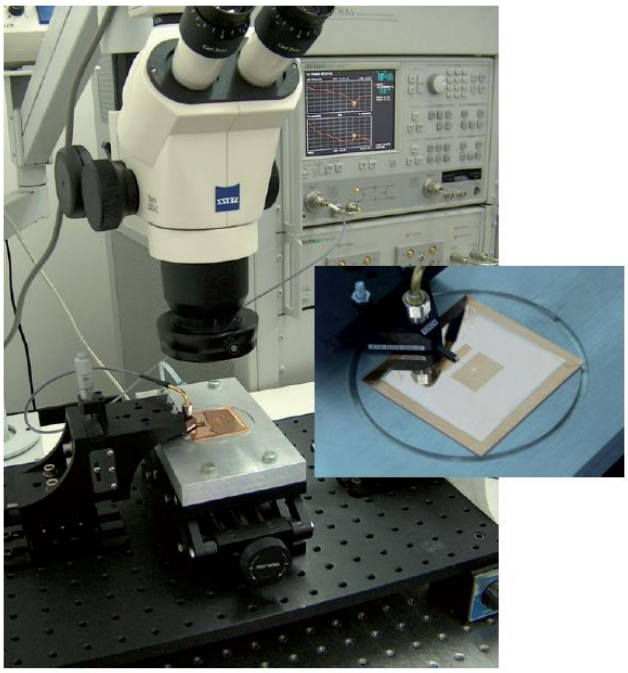

Fig. 2.29. Photograph of the test setup for the experimental characterization of V-band patch antenna on BCB substrate.

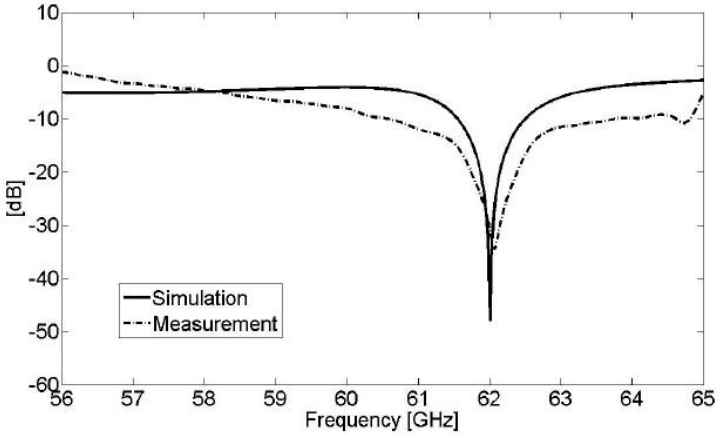

Fig. 2.30. Comparison between simulated and measured return loss of V-band patch antenna on BCB substrate.

3

Millimeter Wave Antennas on BCB Substrate

3.1 Introdution

The effectiveness of BCB polymer as dielectric substrate is further validated by describing the design and experimental test of two different V-band array realized on BCB through the same technological process previously adopted in the fabrication of CBCPW.

3.2 Microstrip V-band Array

The first prototype developed is a V-band microstrip array. The array is composed of 36 slot–fed patch antennas, with an inter–element spacing equal to 0.85 λ_0 at the central design frequency f_0=60 GHz. A schematic view of the array is reported in Fig. 3.1 and the relative parameters dimensions shown in Table 3.1, while a photograph of the created structure, highlighting both the patches layer and the feeding line network, is shown in Fig. 3.2. BCB Cyclotene series 3022 is adopted as substrate layer of thickness h.

Table 3.1. Physical parameters of fabricated V–band array.

Parameter	Value	Specification
W	27.07mm	Array width
L	27.1mm	Array length
Wp	1.85mm	Patch width
Lp	1.41mm	Patch length
d	4.25mm	Inter-element spacing
h	26μm	BCB substrate height

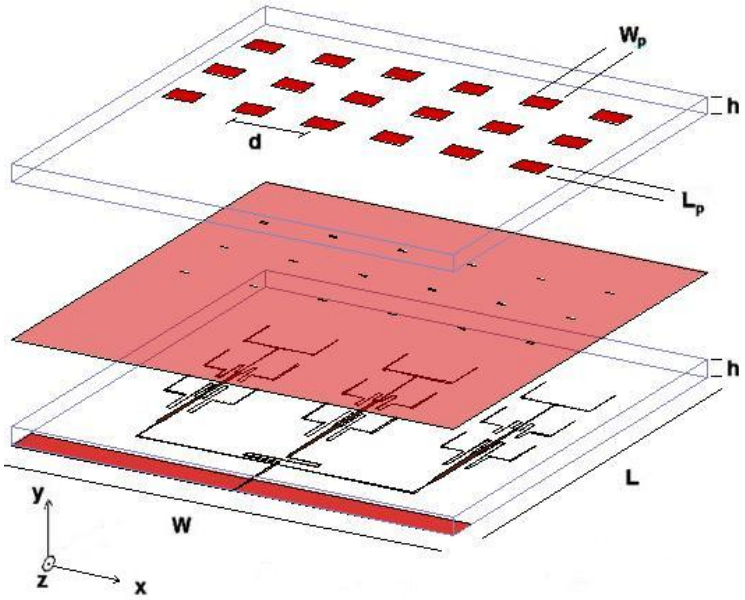

Fig. 3.1. Schematic view of V–band array of slot–fed patch antennas on BCB substrate.

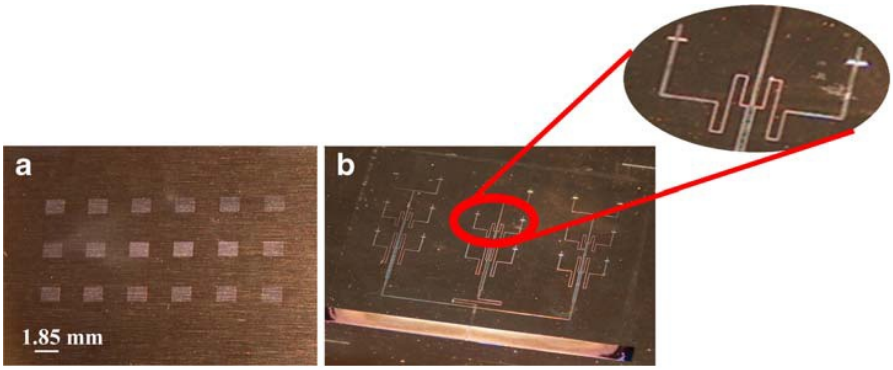

Fig. 3.2. Photographs of fabricated V–band array: (a) patches layer and (b) feeding network.

The millimeter–wave patch array is firstly tested (Fig. 3.3) by measuring the return loss, reported in Fig. 3.4, where a satisfactory agreement with simulated data from Ansoft HFSS [13] can be observed. When compared to the simulation results, measured data show a resonance minimum of about -26 dB closer to the design frequency $f_0 = 60$ GHz and a larger -10 dB impedance

bandwidth, approximately going from 59.5 GHz to 62 GHz. Uncertainties in the probe contact are probably responsible for the deviation between the measured and the simulated return loss in the range from 60 GHz to 65 GHz.

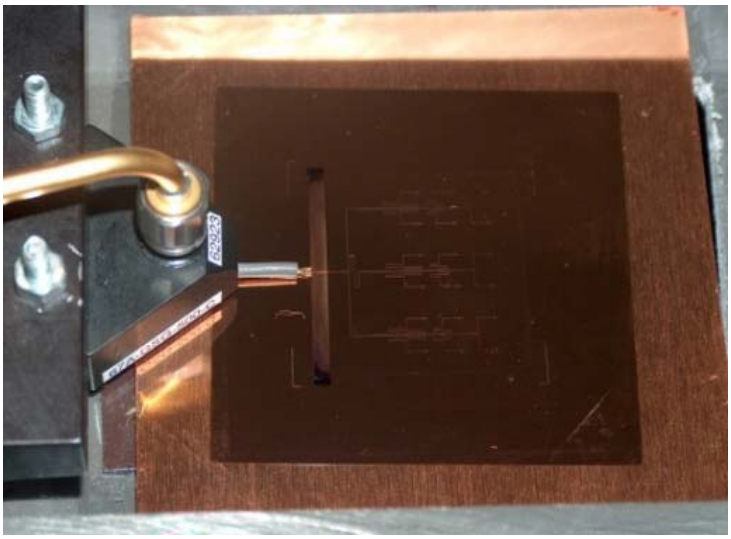

Fig. 3.3. Picture of V-band array under test.

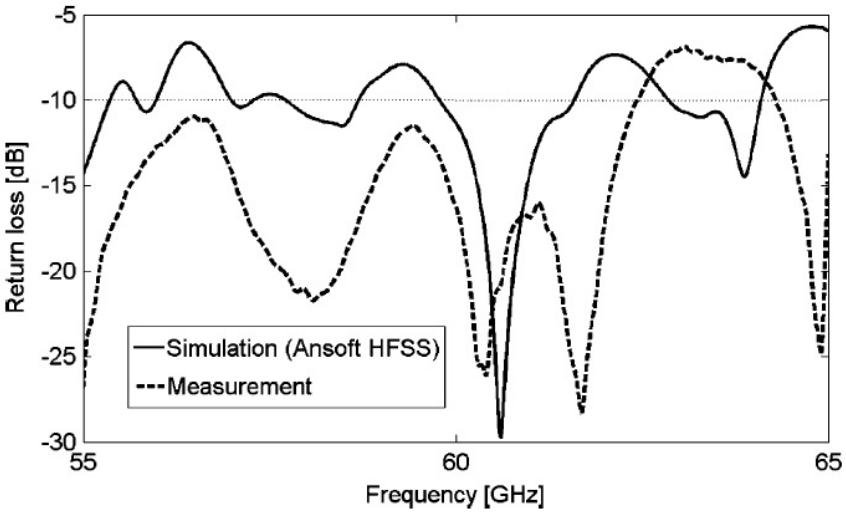

Fig. 3.4. Return loss of V–band array on BCB substrate: comparison between simulation and measurement.

Near–field measurements are performed at various frequencies on a square grid having side of about 10 cm, at a distance of 40 mm from a standard V–band rectangular waveguide used as probe (Fig. 3.5), with a sampling spacing equal to $\lambda_0/2$ on both directions at the central frequency f_0=60 GHz. The contour plot of the normalized nearfield amplitude at 60 GHz is reported in Fig. 3.6 and Fig. 3.7.

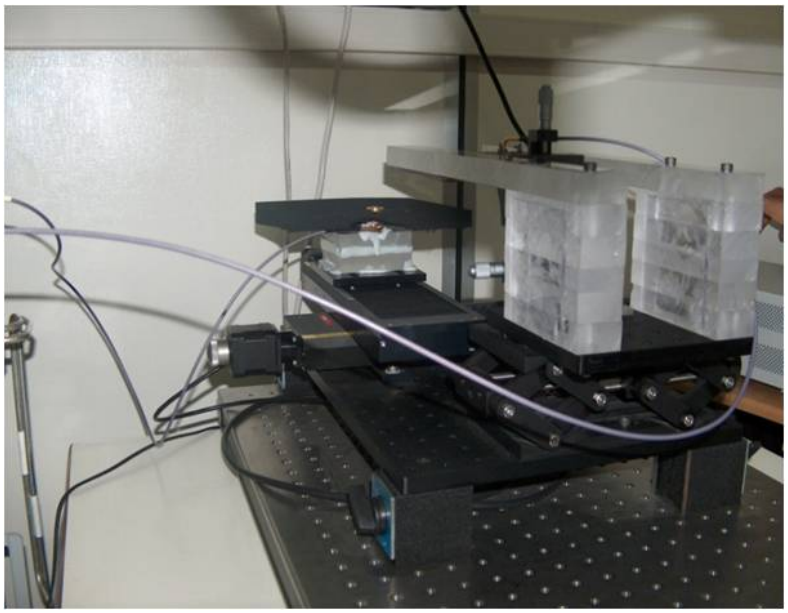

Fig. 3.5. Setup of the prototype pattern measurement.

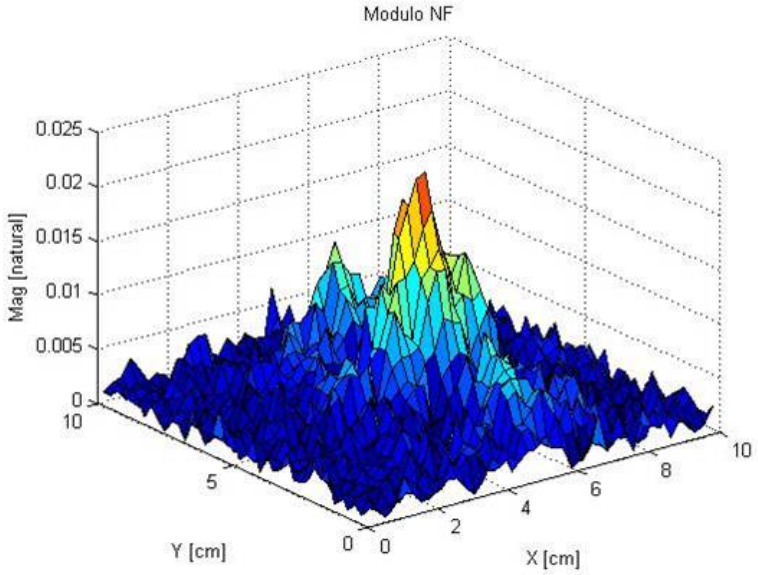

Fig. 3.6. Normalized near–field amplitude of V–band array at 60 GHz (3D).

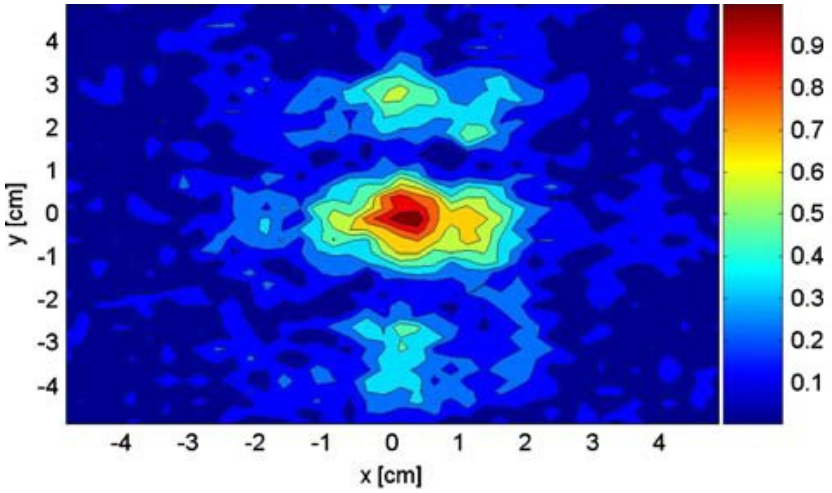

Fig. 3.7. Normalized near–field amplitude of V–band array at 60 GHz.

The planar near–field to far–field transformation [19] is applied to the measured data for obtaining the array radiation pattern, whose results at 60

GHz for the H–plane and the E–plane are reported in Fig. 3.8 and successfully compared with the exact theoretical fields.

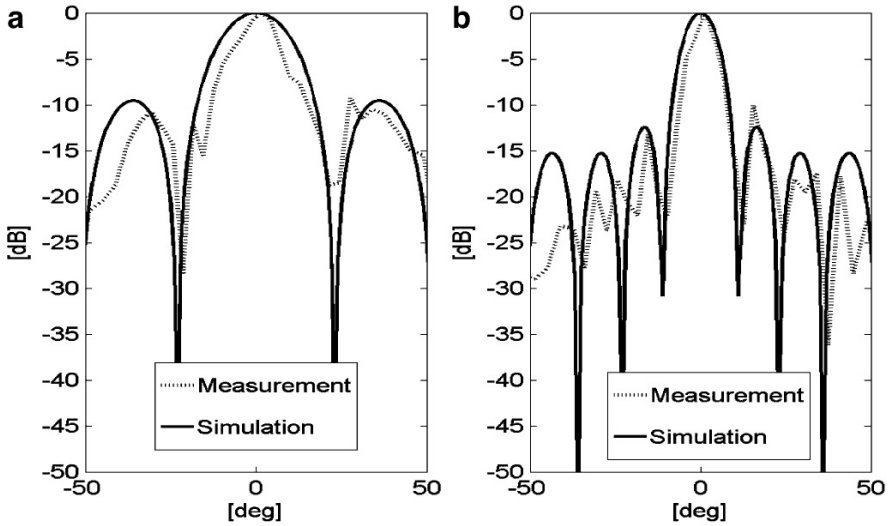

Fig. 3.8. Far–field radiation pattern of V–band array: (a) H–plane and (b) E–plane.

As a final validation, the boresight gain of V–band array is experimentally characterized by adopting the Friis transmission formula [20] with two calibrated 5075 GHz horn antennas Model 261 V. An average value of about 20 dB can be observed in the measured gain curve of Fig. 3.9, with a maximum of about 22 dB in the frequency range approximately going from 60.5 GHz to 63 GHz, strictly close to the interval within which an optimum matching is displayed by the return loss of Fig. 3.4.

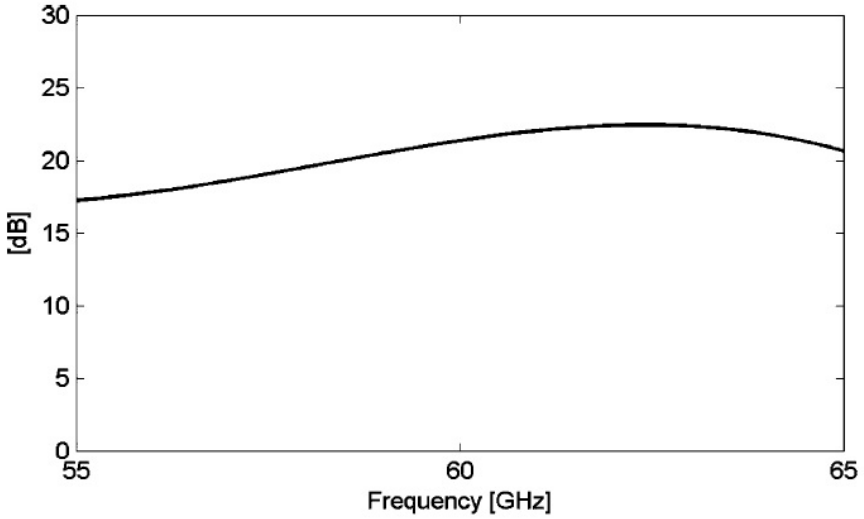

Fig. 3.9. Measured boresight gain of V–band array on BCB substrate.

3.3 Millimeter–Wave Reflectarray Antenna

In this Section, the use of BCB is extended to the design of a millimeter–wave reflectarray antenna. The reflectarray configuration is based on the use of variable size patches printed on a BCB dielectric substrate. The analysis of the single reflecting element is performed by a full–wave commercial code satisfying the infinite array condition.

In order to properly choose the substrate thickness d to be used in the design of a 60 GHz reflectarray, parametric simulations are executed by varying the substrate height d in the range from 26 μm to 130 μm.

The design curves depicted in Figs. 3.10–3.11 represent the reflection coefficient of an infinite array of identical elements illuminated by a normally incident plane wave. For each value of the parameter d, the patch length is varied around the corresponding resonant size.

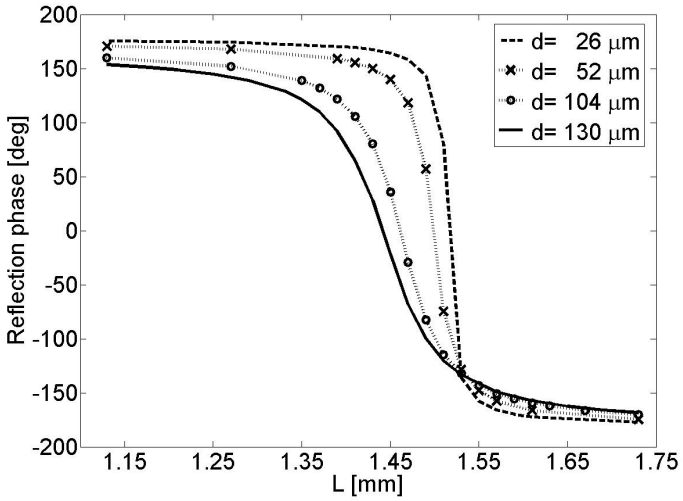

Fig. 3.10. Phase design curves of 60 GHz reflectarray on BCB substrate.

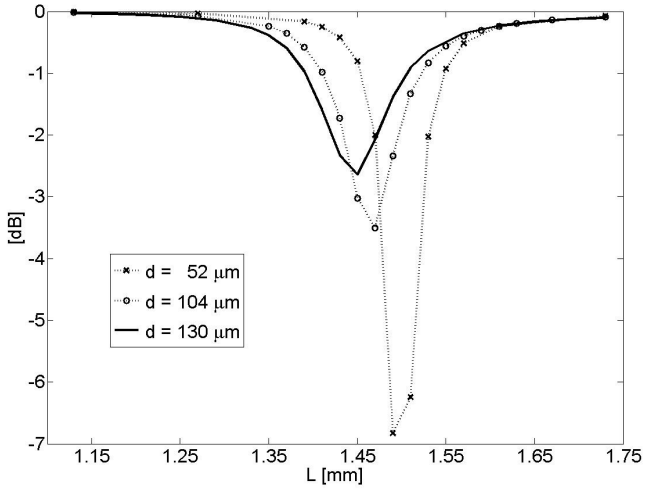

Fig. 3.11. Amplitude design curves of 60 GHz reflectarray on BCB substrate

It can be observed from Fig. 3.10 that a thicker substrate gives a phase curve with lower sensitivity to the variations of patch length [21]. A smoother phase curve is generally preferred for reflectarray antennas, as giving more

exibility with respect to the fabrication tolerances of available manufacturing processes.

For the examined case of 60 GHz reflectarray on BCB substrate, a dielectric slab thickness equal to 130 μm is fixed to meet the constraints on the patch size precision imposed by the adopted fabrication process. This choice also minimizes the dielectric loss [21], as shown by the amplitude curves in Fig. 3.11.

The design curves corresponding to the selected substrate thickness are employed to design a 21 x 21 element reflectarray antenna with a spacing equal to 0.5 λ_0 between each radiating element along both array directions.

The reflecting surface is offset–fed by a pyramidal horn with an aperture size equal to 14.78 mm x 11.63 mm. The feed is placed in the E–plane at a distance of 135 mm from the array surface, with an inclination angle of 18 degrees from the direction normal to the reflecting plane.

The array design is performed by employing a synthesis algorithm [22] based on the iterative projection approach. Each reflectarray element is chosen to properly compensate the phase delay due to the different feed–element paths, so giving a main radiation lobe along the broadside direction.

The complex design curves relative to the different incidence angles from the feed to the various elements are considered in order to accomplish the accurate reflectarray synthesis. Furthermore, the feed pattern (Fig. 3.12) is accurately taken into account into the synthesis algorithm [22].

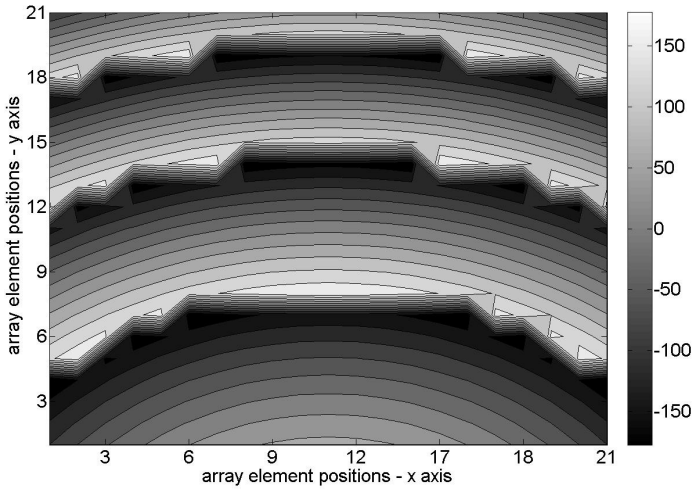

Fig. 3.12. Phase pattern of illuminating feed.

The synthesized reflectarray is realized on a 130 μm thick BCB substrate, by following a three step procedure entirely developed into the Microwave Laboratory at University of Calabria. The BCB is firstly deposited on the copper ground plane, having excellent planarity features, by using the spin coater, and the resulting covered circuit is then cured in a convection oven under nitrogen.

A soft cure process is adopted in this case, due to the multilayer configuration. The top copper layer is then deposited by adopting the Physical Vapor Deposition (PVD) process based on thermal evaporation, and the reflectarray pattern is finally obtained by a classical lithography technique.

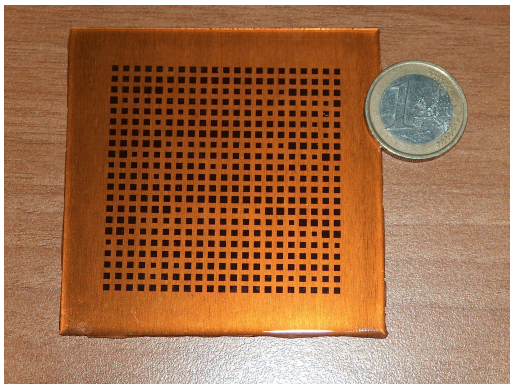

Fig. 3.13. Photograph of 60 GHz reflectarray on BCB substrate.

A photo of the fabricated reflectarray is reported in Fig. 3.13, and a picture of the measurement setup into the anechoic chamber is shown in Fig. 3.14.

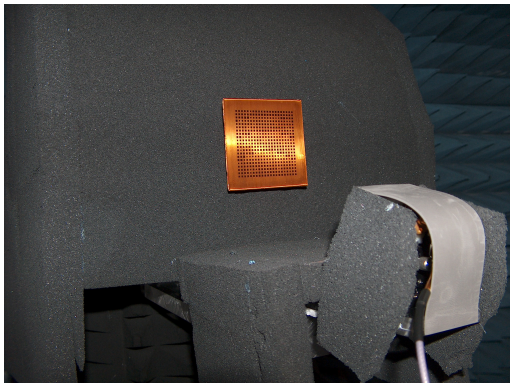

Fig. 3.14. Photograph of measurement setup.

The experimental validation of the reflectarray prototype is performed by near–field measurements on a planar surface placed at a distance of 23 cm from the test antenna, with a sampling spacing equal to $\lambda_0/2$ on both directions at the frequency $f_0 = 60$ GHz.

A standard V–band rectangular waveguide is used as measuring probe. The planar near–field to far–field transformation is applied to the measured data for obtaining the reflectarray radiation pattern shown in Fig. 3.15. A good agreement can be observed with the numerical result obtained from the analysis.

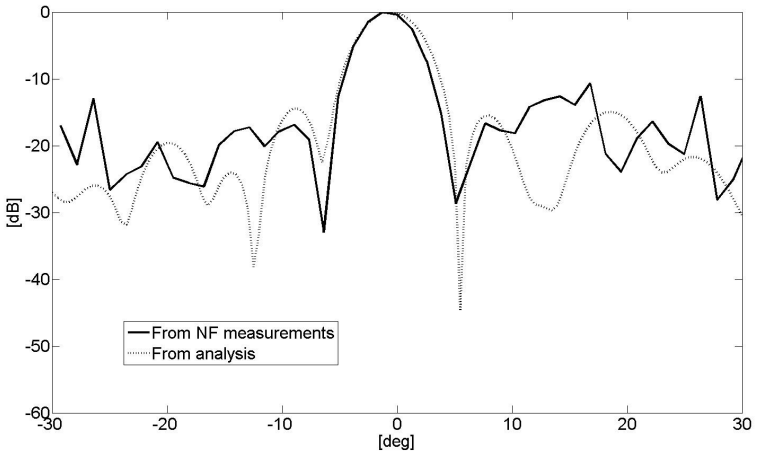

Fig. 3.15. Comparison between measured and simulated E–plane pattern.

To validate the frequency radiation features of reflectarray, the boresight gain is experimentally characterized by adopting the Friis transmission formula with two standard V–band calibrated horn antennas. A maximum value of 29 dB is obtained, and a 1 dB variation can be observed within a large frequency band between 58 GHz and 62 GHz (Fig. 3.16).

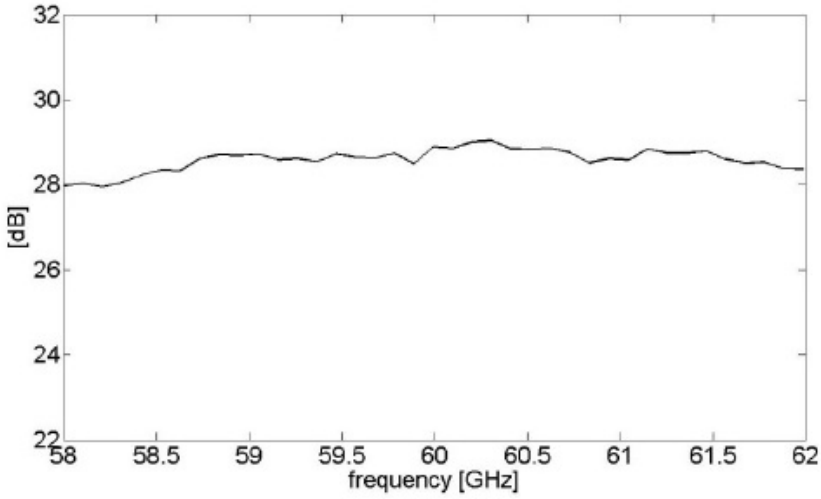

Fig. 3.16. Reflectarray boresight gain vs. frequency.

4

Micromachined Millimeter-Wave Antennas

4.1 Introduction

The actual trend toward compact device systems, combining circuit boards or packages with antennas, induces the investigation of processing technologies able to realize a simple integration while maintaining high–performance, low–cost, and easy characterization. A strong requirement for a complete on–package integration is to realize antennas and feeding lines with the same processing technique as that adopted for circuits boards. The microstrip line certainly gives the simplest structure for this purpose, however it has significant metallic and dielectric losses.

Moreover, it can radiate at discontinuities, thus giving a low polarization purity. As a consequence, the efficiency of this technology is low, with significant drawbacks at frequencies over K-bands. On the other hand, waveguide slot arrays [23] can be used to design high-performance antennas with low losses and high polarization purity. As such, they are very popular antennas for K-bands and over, but the main drawback is the need of complex transitions to integrate them into planar circuits [24], [25].

Typical integration schemes are bulky and usually require a precise machining process, with a fine–tuning mechanism difficult to achieve at millimeter frequencies. A straightforward solution would be the complete integration of the rectangular waveguides of the slot array into the microstrip substrate. This would assure a significant reduction in the waveguides bulk while leading to use standard processing techniques for the realization of the entire structure. On the basis of these motivations, substrate integrated waveguide (SIW) technology has been proposed in recent years [26], [27], soon becoming very popular among the scientific community. A strong disadvantage of SIW is related to the fact that it is unable to match the performances of a true rectangular waveguide array, as its propagation characteristics cannot be computed with high accuracy and specific analysis techniques are required.

In this Chapter, a new integrated platform is presented, which synthesizes the waveguide slot array on the same substrate of the exciting microstrip line, with the two dissimilar components oriented along the same axis (Fig. 4.1).

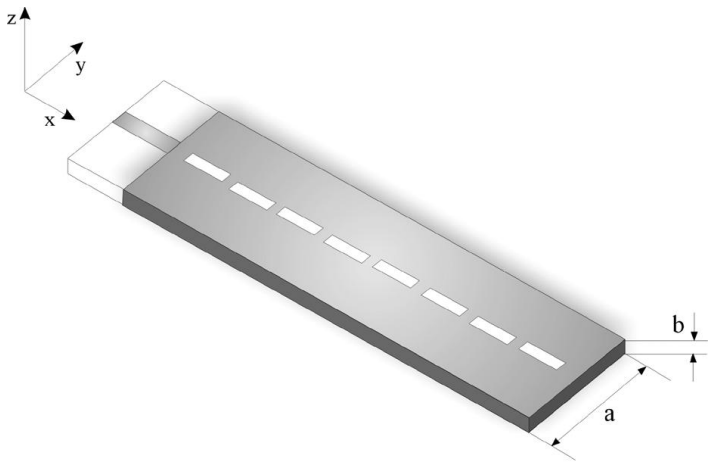

Fig. 4.1. Layout of linear slot array integrated on waveguide.

The rectangular waveguide is directly machined into the dielectric substrate of the feeding microstrip line by using two metallized grooves, and the radiating slots are etched on the upper ground plane. A single planar fabrication technique is adopted to realize the entire structure, thus guaranteeing excellent mechanical tolerances as well as a tuning–free design. The slot array synthesis is performed by a specific procedure basically adopting Elliotts approach [28], but properly developed for the accurate design of the proposed structure. Both numerical and experimental validations on a linear array are discussed to show the effectiveness of the approach.

4.2 Synthesis Procedure of Slot Array

Standard waveguide slot arrays can be accurately designed by adopting Elliotts technique for the computation of both the slot self–admittance and the external mutual coupling [28]. This procedure can be directly applied to the proposed structure in Fig. 4.1 by following the approach outlined in [29].

The slot self–admittance is evaluated by a full–wave analysis based on the method of moments (MoM), allowing also to take exactly into account for the thickness of the metallic walls within which the radiating slots are cut. Entire domain basis functions are used to develop an accurate procedure adopting a spatial domain approach for the computation of the internal Greens function [30].

The external mutual coupling is exactly equal to that obtained in the standard case of empty waveguides [31]. Due to the smallness of waveguide height in the proposed slot array (Fig. 4.1), the radiating slots are not true shunt admittances, as required by the standard approach [28]. This is a significant difference to be taken into account. The standard model of a $\lambda_g/2$ waveguide section, with a single radiating slot, is composed by two $\lambda_g/4$ transmission line sections, with a shunt admittance Y_S modeling the slot [32] (Fig. 4.2).

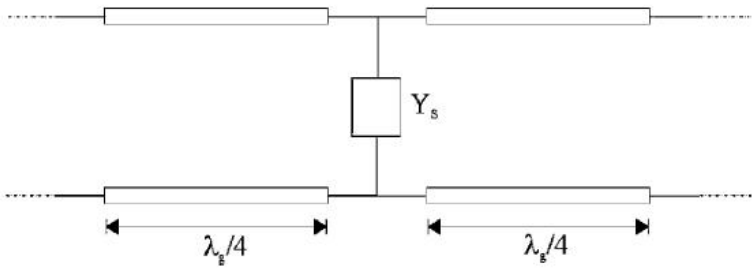

Fig. 4.2. Standard model of a $\lambda_g/2$ waveguide section with a single radiating slot modeled as a shunt admittance Y_s.

For the proposed slot array in Fig. 4.1, this model is not accurate enough, but two additional reactances can be simply introduced to improve it, thus replacing the single shunt admittance Y_S with a T–network, as reported in Fig. 4.3.

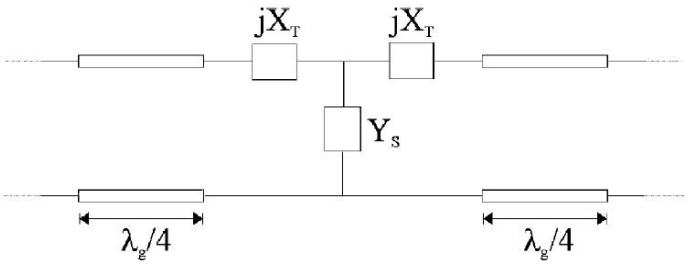

Fig. 4.3. Standard model of a $\lambda_g/2$ waveguide section with a single radiating slot modeled as a T–network.

Both admittance Y_S and reactance X_T can be easily extracted from MoM analysis of the slot. The above changes in the circuit model give a scattering matrix well matching the actual slot response. On the basis of the above

considerations, the equivalent circuit of the short-circuited linear slot array in Fig. 4.1 can be modeled as reported in Fig. 4.4.

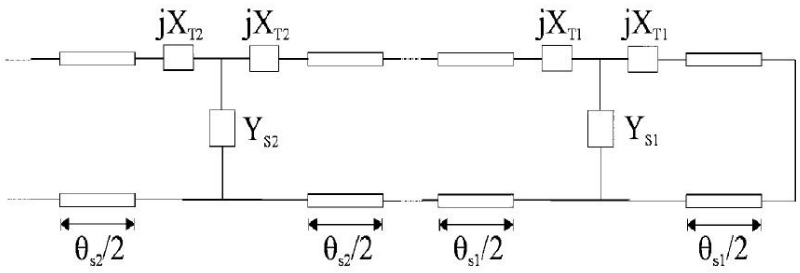

Fig. 4.4. Equivalent circuit of linear slot array in Fig. 4.1.

Even if different from the circuit model given by Elliotts approach [32], it can be simply rearranged by replacing each section of transmission line and relative T–network with a single transmission line having a different length. Length changes θ_{Si}(Fig. 4.1), i=1,2,...,N, N being the number of radiating slots, are computed by implementing an iterative synthesis procedure with a two-step strategy.

As the mutual coupling is quite small in a linear array, the slot length and the offsets are first derived by assuming the shunt model of Fig. 4.2. Then, the actual T–network (Fig. 4.3) is derived for each slot, and the new transmission lines lengths are obtained. Finally, the external mutual coupling is computed with the proper slot spacing, as given by the correction step.

4.3 Experimental Results

The synthesis procedure above outlined is applied to design a linear slot array of eight elements by imposing a −20dB Taylor pattern on the zx plane (Fig. 4.1). Taylor one–parameter method is adopted to determine the excitation coefficients giving the prescribed field. However, the discretization of the method, more applicable to continuous–line source distribution, produces the first sidelobe around 2 dB lower than the specified −20dB level [33]. A spacing equal to $\lambda_g/2$ is initially fixed between adjacent slots at the central frequency $f_0 = 8$GHz.

As illustrated in Fig. 4.1, the waveguide array is terminated into a short circuit, located at a distance equal to $\lambda_g/4 + \lambda_g/2$ from the last radiating slot. The waveguide is machined into a dielectric substrate having relative dielectric constant $\varepsilon_r = 2.33$. To guarantee the fundamental TE_{10} mode propagation, while inhibiting the excitation of higher order modes, the transverse section is

dimensioned to have width a = 15mm and height b = 0.762mm. A thickness equal to 0.035mm is fixed for the metallic walls. In the first step of the iterative synthesis procedure, a unitary normalized input admittance is imposed by assuming a shunt admittance model (Fig. 4.2) for the radiating slots.

The computed slot admittance values are then used to obtain the slots lengths and the offsets reported in Table 4.1. In a subsequent step, the improved T–network model (Fig. 4.3) is assumed for the radiating slots, and the corrected values of the slot spacings reported in Table 4.1 are derived.

Table 4.1. Positions, Dimensions, and Spacings of Radiating Slots

# Slot	Offset [mm]	Length [mm]	Initial slot spacing [mm]	Corrected slot spacing [mm]
1	-0.1036	17.940	θ_{S1}=32.03625 ($3\lambda_g/4$)	θ_{S1}=32.03625 ($3\lambda_g/4$)
2	0.1928	17.982	θ_{S2}=21.3575 ($\lambda_g/2$)	θ_{S2}=21.95
3	-0.2646	18.088	θ_{S3}=21.3575 ($\lambda_g/2$)	θ_{S3}=21.95
4	0.3081	18.186	θ_{S4}=21.3575 ($\lambda_g/2$)	θ_{S4}=21.95
5	-0.3081	18.186	θ_{S5}=21.3575 ($\lambda_g/2$)	θ_{S5}=21.95
6	0.2646	18.088	θ_{S6}=21.3575 ($\lambda_g/2$)	θ_{S6}=21.95
7	-0.1928	17.982	θ_{S7}=21.3575 ($\lambda_g/2$)	θ_{S7}=21.95
8	0.1036	17.940	θ_{S8}=21.3575 ($\lambda_g/2$)	θ_{S8}=21.3575 ($\lambda_g/2$)

The synthesized linear arrays with parameters reported in Table 4.1 (before and after the correction of the slot spacing) are realized, and a microstrip transition is properly introduced to guarantee the matching between the waveguide input and the 50-Ω microstrip feeding line. A photograph of the complete array structure mounted into the anechoic chamber of the Microwave Laboratory at the University of Calabria is reported under Fig. 4.5.

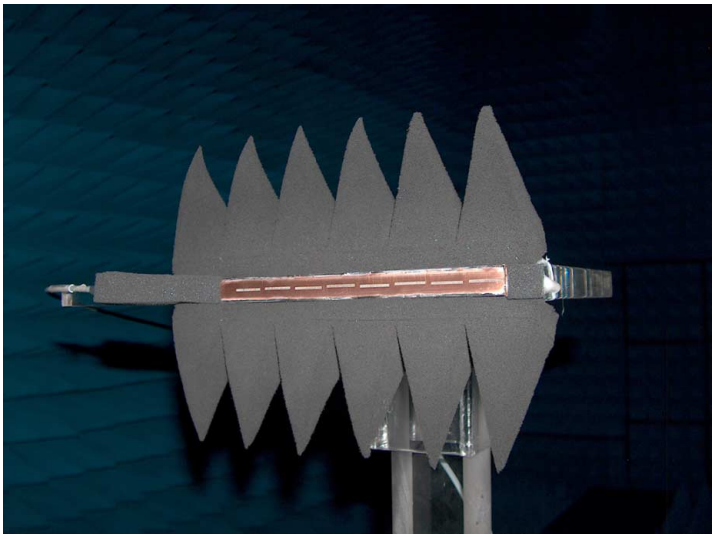

Fig. 4.5. Photograph of fabricated linear slot array with dimensions as in Table 4.1 after the correction of the slot spacings.

First, the experimental characterization of the return loss is performed, and the measurement result illustrated in Fig. 6 shows a very good impedance matching of about -40dB in the proximity of the central frequency $f_0 = 8$GHz for the final array configuration (T–network model) derived from the design stage.

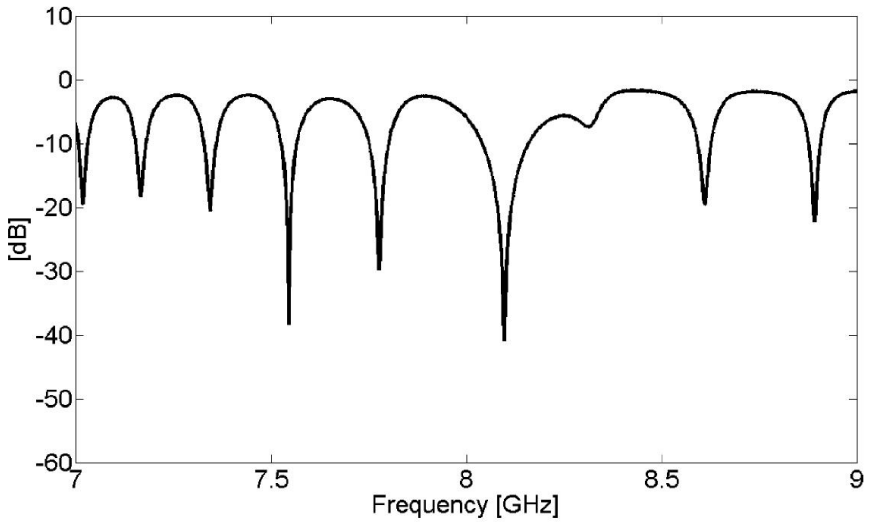

Fig. 4.6. Measured return loss of linear slot array with dimensions as in Table 4.1 after the correction of the slot spacings.

The slight frequency shift with respect to the fixed design frequency $f_0 =$ 8GHz can be partially attributed to realization tolerances, but it is mainly due to the fact that the microstrip transition effect is not included into the structure model adopted in the synthesis procedure.

To demonstrate the effectiveness of the two–step synthesis procedure, a frequency characterization of the radiation features is performed on the two fabricated arrays. Far–field measurements at various frequencies are executed into the anechoic chamber of the Microwave Laboratory at the University of Calabria by adopting as the measuring probe a WR–137 rectangular waveguide operating within the range from 5.85 to 8.2 GHz. A photograph of the measurement setup showing both the array and the probe is shown in Fig. 4.7.

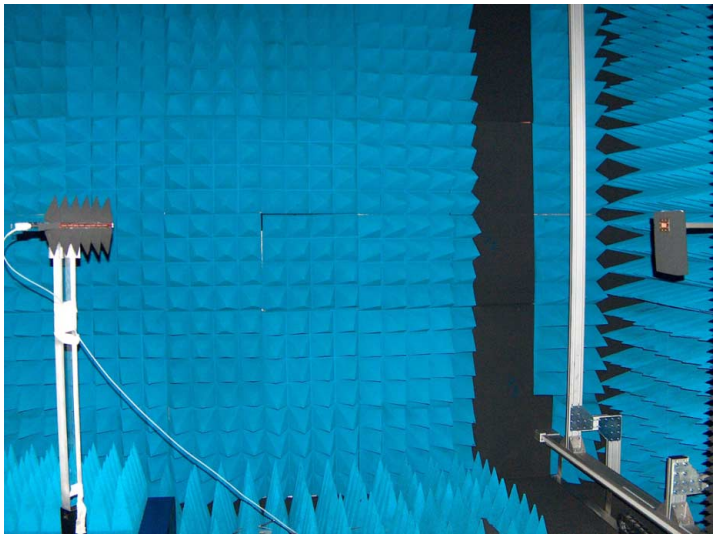

Fig. 4.7. Measurement setup into the anechoic chamber at University of Calabria.

A better agreement between measured and predicted (synthesis) far–field patterns at the design frequency $f_0 = 8$GHz (Figs. 8 and 9) is clearly evident for the array synthesized with the improved T–network model (Fig. 9). In this case, a more similar agreement with the pattern obtained in the synthesis stage can be observed at different frequencies around the design value of 8GHz (Fig. 10).

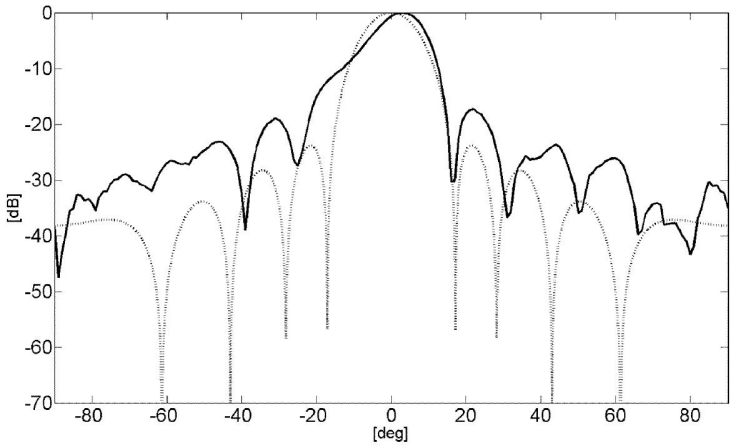

Fig. 4.8. Far–field pattern (zx plane) of slot array in Table 4.1 with the initial slot spacings equal to $\lambda_g/2$ (shunt-admittance model) at 8GHz: comparison between measurement (solid line) and synthesis (dotted line).

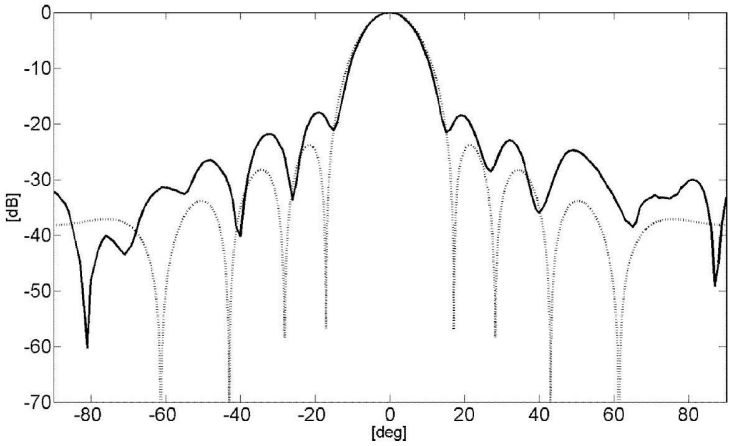

Fig. 4.9. Far–field (*zx* plane) pattern of slot array in Table 4.1, after the correction of the slot spacings (T–network model), at 8GHz: comparison between measurement (solid line) and synthesis (dotted line).

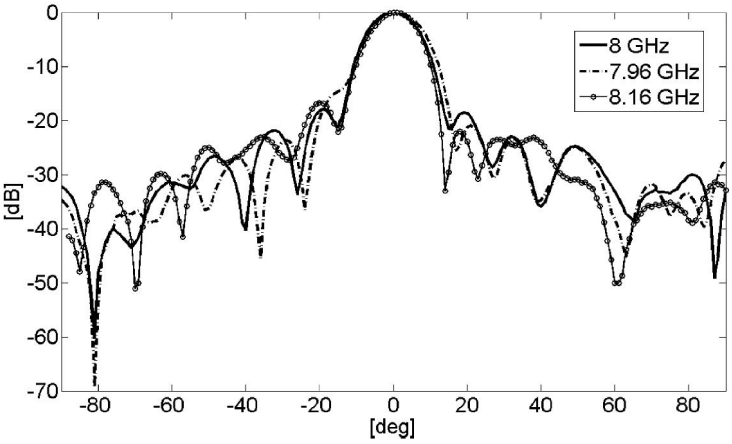

Fig. 4.10. Measured far–field (*zx* plane) pattern of slot array in Table 4.1, after the correction of the slot spacings (T–network model), at various frequencies.

To complete the experimental characterization, the boresight gain of the final array configuration in Table 4.1, after the correction of the slot spacings, is measured by adopting the three–antenna method [20].

First, the gain of the WR–137 rectangular waveguide used as probe is derived from transmission measurements between two identical waveguides. A value of about 8dB in the range between 7 and 9 GHz is obtained for the

measuring probe. This quantity is then used to derive the maximum gain of the slot array within the same frequency range. A maximum value of about 12dB can be observed in Fig. 11, with a −3dB bandwidth approximately going from 7.96 to 8.32 GHz. A good agreement is also shown with the result obtained from HFSS simulations. Differences between experimental and simulated gain are probably due to measurement errors and realization tolerances.

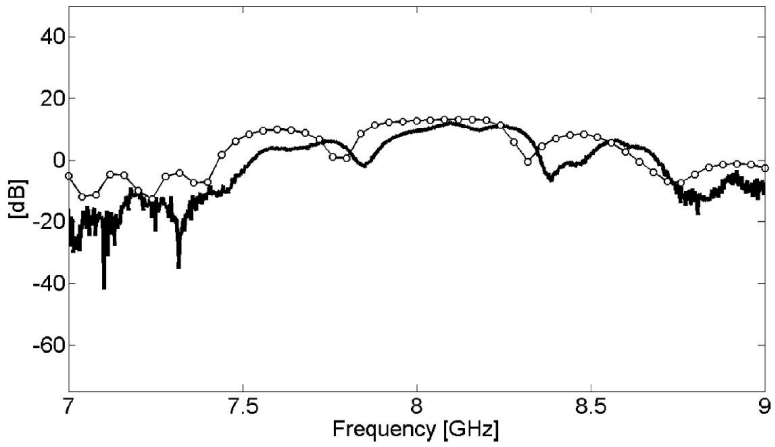

Fig. 4.11. Boresight gain versus frequency for slot array in Table 4.1, after the correction of the slot spacings (T–network model): comparison between measurement (solid line) and HFSS simulation (circles).

5

Conclusions

The development of innovative techniques for the realization of millimeter-wave printed circuits has been discussed in this PhD thesis.

A new polymeric material, named Benzocyclobutene (BCB), has been proposed as low losses and frequency stable dielectric substrate for devices operating up to millimeter frequency values.

An in-house manufacturing technology has been developed for the realization of BCB-based microstrip structures. The developed process has been successful adopted for the fabrication of several millimeter-wave prototypes of arbitrary thickness, showing a very high degree of accuracy.

Furthermore, the proposed technology has proved to be easily deployable and less expensive than the nanotechnology, usually adopted in the integrated electronics industry.

An accurate experimental characterization of the BCB dielectric properties has been performed within the range from 11 GHz to 65 GHz, through a CBCPW test structure realized at the Microwave Laboratory of the University of Calabria. A steady permittivity value of about 2.65 and low loss tangent ranging from 0.001 up to 0.009 have been derived from measurements.

These parameters have been adopted to design several millimeter-wave antenna prototypes, including a V-band slot-fed array and a 60 GHz reflectarray.

The synthesized antennas have been successful realized and measured, showing the effectiveness of the developed manufacturing technology as well as the good performances of BCB as millimeter wave dielectric substrate.

Finally, a micromachined millimeter wave antenna, based on a waveguide slot array placed on the same substrate of the feeding microstrip line, has

been realized. The antenna has been tested in the anechoic chamber of the University of Calabria, showing good performances.

References

1. Kao-Cheng Huang, David J. Edwards, Millimetre Wave Antennas for Gigabit Wireless Communications, Wiley, 2008.
2. Dow Chemical Company (http://www.dow.com).
3. Dow Chemical Company Datasheet: Processing Procedures for Dry-Etch Cyclotene Advanced Electronics Resins (Dry-Etch BCB).
4. Dow Chemical Company Datasheet: Processing Procedures for Cyclotene 3000 Series Dry Etch Resins.
5. I. Venneri, Antenne planari per applicazioni a frequenze millimetriche, University of Calabria, 2005.
6. Di Donald M. Mattox, Handbook of physical vapor deposition (Pvd) processing: film formation, adhesion, surface preparation and contamination control, 1998.
7. Dow Corning, Sylgard 184 Silicone Elastomer (http://www.dowcorning.com), 2007.
8. N. Tiercelin, P. Coquet, R. Sauleau, V. Senez, H. Fujita, Polydimethylsiloxane membranes for millimeter–wave planar ultra flexible antennas, J. Micromech. Microeng., 2006.
9. HD MicroSystems, PI-2525, PI-2555, PI-2556 and PI-2574 Polyimide (http://www2.dupont.com), 2008.
10. MicroChem, SU–8 Permanent Photoresists (http://www.microchem.com/products/su_eight.htm).
11. F. D. Mbairi, H. Hesselbom, High frequency design and characterization of SU–8 based conductor backed coplanar waveguide transmission lines, Proc. Int. Symp. on Advanced Packaging Materials: Processes, Properties and Interfaces, pp. 243248, 2005.
12. Dow Chemical Comp, CYCLOTENE 3000 Series Advanced Electron Resins (http://www.dow.com/cyclotene), 2005.
13. Ansys HFSS Software (http://www.ansys.com/Products/Simulation+Technology/Electromagnetics/High-Performance+Electronic+Design/ANSYS+HFSS)
14. D. C. DeGroot, D. K. Walker, R. B. Marks, Impedance mismatch effects on propagation constant measurements, Proc. 1996 IEEE Conf. Packag., pp. 141–143, 1996.
15. Y. Eo, W. R. Eisenstadt, High–speed VLSI interconnect modeling based on S–parameter measurements, IEEE Trans. Comp., Hybrids and Manufact. Tech., 16, 1993.

16. G. Ghione, C. Naldi, Parameters of coplanar waveguides with lower ground plane, IEE Electronics Letters, 19, 1983.
17. E. Hammerstad, O. Jensen, Accurate models for microstrip computer–aided design, Proc. IEE MTTSymp, pp. 407-409, 1980.
18. R. E. Collin, Foundations for microwave engineering, McGraw–Hill, New York, 1992.
19. J. J. H Wang, An examination of the theory and practices of planar near–field measurement, IEEE Trans. on Antennas and Propag., 36, 1988.
20. C. A. Balanis, Antenna theory: analysis and design. John Wiley and Sons, New York, 1997.
21. D.M. Pozar, S.D. Targonski, H.D. Syrigos, Design of millimeter wave microstrip reflectarrays, IEEE Trans. Antennas Propag., 45, 1997.
22. F. Venneri, S. Costanzo, G. Di Massa, G. Angiulli, An improved synthesis algorithm for reflectarrays design, IEEE Antennas Wireless Propag. Lett., 4, 2005.
23. R. C. Johnson and H. Jasik, Antenna Engineering Handbook. New York: McGraw-Hill, 1984.
24. J. Frey and K. Bhasin, Microwave Integrated Circuits. Norwood, MA: Artech House, 1985.
25. J. S. Izadian and S. M. Izadian, Microwave Transition Design. Norwood, MA: Artech House, 1988.
26. D. Deslandes and K.Wu, "Integrated microstrip and rectangular waveguide in planar form", IEEE Microw. Wireless Compon. Lett., vol. 11, no. 2, pp. 6870, Feb. 2001.
27. M. Clenet, J. Litzenberger, D. Lee, S. Thirakoune, G. A. Morin, and Y. M. M. Antar, "Laminate waveguide as radiating element for array applications", IEEE Trans. Antennas Propag., vol. 54, no. 5, pp. 14811487, May 2006.
28. R. S. Elliott, "An improved design procedure for small arrays of shunt slots", IEEE Trans. Antennas Propag., vol. AP-31, no. 1, pp. 4853, Jan. 1983.
29. G. A. Casula, G. Mazzarella, and G. Montisci, "Design of slot arrays in a waveguide partially filled with a dielectric slab", Electron. Lett., vol. 42, no. 13, pp. 730731, 2006.
30. G. Mazzarella and G. Montisci, "A rigorous analysis of dielectric-covered narrow longitudinal shunt slots with finite wall thickness", Electromagnetics, vol. 19, pp. 407418, 1999.
31. G. Mazzarella and G. Panariello, "On the evaluation of mutual coupling between slots", IEEE Trans. Antennas Propag., vol. AP-35, no. 11, pp. 12891293, Nov. 1987.
32. T. V. Khac and C. Carson, "Impedance properties of a longitudinal lot antenna in the broad face of a rectangular waveguide", IEEE Trans. Antennas Propag., vol. AP-21, no. 5, pp. 708710, Sep. 1973.
33. C. Phongcharoenpanich, T. Lertwiriyaprapa, and M. Krairiksh, "A comparative study of the discrete array pattern synthesis providing the tapered minor lobes", in Proc. IEEE AP-S Int. Symp., 2000, pp. 12261229.

6

Publications

Book Chapters

1. S. Costanzo, G. Di Massa, M. Pastorino, A. Randazzo, **A. Borgia**, *Non-Invasive Microwave Characterization of Dielectric Scatterers*, in ***Microwave Materials Characterization***, Sandra Costanzo, **INTECH**, 2012.

Journals

1. F. Venneri, S. Costanzo, G. Di Massa, E. Marozzo, **A. Borgia**, P. Corsonello, *Beam-Scanning Reflectarray Based on a Single Varactor-Tuned Element*, **International Journal of Antennas and Propagation**, 2012.

2. S. Costanzo, F. Venneri, **A. Borgia**, I. Venneri, G. Di Massa, *60 GHz microstrip reflectarray on a benzocyclobutene dielectric substrate*, **IET Science, Measurement** & **Technology**, 2011, Vol.5, pp. 134-139, ISSN: 1751-8822.

3. S. Costanzo, **A. Borgia**, I. Venneri, G. Di Massa, *Millimeter-Wave Structures on Benzocyclobutene Dieletric Substrate*, **Radioengineering**, 2011, Vol.20, pp. 785-789, ISSN: 1210-2512.

4. G. Amendola, E. Arnieri, L. Boccia, **A. Borgia**, P. Focardi, I. Russo, *Hybrid waveguide-stripline feeding network for dual polarised array at K band*, **IET Microwaves, Antennas** & **Propagation**, 2011, Vol.5, pp. 1568-1575, ISSN: 1751-8725.

5. S. Costanzo, I. Venneri, G. Di Massa, **A. Borgia**, *Benzocyclobutene as substrate material for planar millimeter-wave structures: dielectric cha-*

racterization and application, **International Journal of Infrared, Millimeter and Terahertz Waves**, 2010, Vol.31, pp. 66-67, ISSN: 1866-6892.

6. G. Di Massa, S. Costanzo, I. Venneri, **A. Borgia**, *New technologies for antenna designer in the millimeter range*, **Atti della Fondazione "Giorgio Ronchi"**, 2010, ISSN: 0391-2051.

7. S. Costanzo, G. A. Casula, **A. Borgia**, G. Montisci, I. Venneri, G. Di Massa, G. Mazzarella, *Synthesis of Slot Arrays on Integrated Waveguides*, **IEEE Antennas and Wireless Propagation Letters**, 2010, Vol.9, pp. 962-965, ISSN: 1536-1225.

8. G. Amendola, E. Arnieri, L. Boccia, **A. Borgia**, I. Russo, *Hybrid Waveguide-Stripline Arrays at K Band*, **Electronics Letters**, 2009, Vol.45, n. 23, pp. 1173-1174, ISSN: 0013-5194.

Conferences

1. F. Venneri, S. Costanzo, G. Di Massa, E. Marozzo, **A. Borgia**, *Implementation of a Full-Range Varactor Tuned Element for the Design of a Reconfigurable Reflectarray*, **RiNEm 2012**, **Rome**, **Italy**, September 2012.

2. F. Venneri, S. Costanzo, G. Di Massa, **A. Borgia**, P. Corsonello, *Design of a Reconfigurable Reflectarray Based on a Varactor Tuned Element*, **EuCap 2012**, **Prague**, **Czech Republic**, March 2012.

3. G. Aloi, **A. Borgia**, S. Costanzo, G. Di Massa, E. Natalizio, V. Loscri', P. Pace, F. Spadafora, *Software Defined Radar: synchronization issues and practical implementation*, **CogArt 2011**, **Barcelona**, **Spain**, October 2011.

4. G. Di Massa, S. Costanzo, **A. Borgia**, I. Venneri, G. Galati, M. Leonardi, E. Piracci, *Multiple Sources Discremination by Array Processing*, **EuCap 2011**, **Rome**, **Italy**, April 2011.

5. G. Di Massa, S. Costanzo, **A. Borgia**, F. Venneri, I. Venneri, *Innovative dieletric materials at millimeter-frequencies*, **ICECom 2010**, **Dubrovnik**, **Croatia**, September 2010.

6. **A. Borgia**, S. Costanzo, G. Di Massa, F. Venneri, I. Venneri, *Design and realization of millimeter-wave reflectarrays on innovative dielectric substrate*, **RiNEM 2010**, **Benevento**, **Italy**, September 2010.

7. **A. Borgia**, G.A. Casula, S. Costanzo, G. Di Massa, G. Mazzarella, G. Montisci, I. Venneri, *A Synthesis Technique for the Design of a Slot Array on Integrated Waveguides*, **RiNEM 2010**, **Benevento**, **Italy**, September 2010.

8. G. Di Massa, S. Costanzo, I. Venneri, **A. Borgia**, G. Mazzarella, G. Montisci, A. Casula, *Slot Arrays on Integrated Micromachined Waveguides*, **EuCap 2010**, **Barcelona**, **Spain**, April 2010.

9. I. Russo, E. Arnieri, **A. Borgia**, G. Amendola, L. Boccia, S. Costanzo, *Dual polarization Ka-Band array with hybrid series/parallel E-Plane waveguide/stripline feeding networks*, **IEEE Symposium on Antennas and Propagation 2009**, **Charleston**, **USA**, June 2009.

10. E. Arnieri, I. Russo, L. Boccia, **A. Borgia**, G. Amendola, *Hybrid waveguide-stripline feeding networks for Ka band and millimeter wave arrays*, **EuCap 2009**, **Berlin**, **Germany**, March 2009 [**Invited**].

11. S. Costanzo, I. Venneri, G. Di Massa, **A. Borgia**, *New technologies and antennas design concepts at millimeter-wave bands*, **EuCap 2009**, **Berlin**, **Germany**, March 2009 [**Invited**].

12. I. Venneri, **A. Borgia**, L. Boccia, G. Amendola, G. Di Massa, *Millimeter waves patch antennas design and realization on BCB polymer sub-strates*, **IEEE Symposium on Antennas and Propagation**, **San Diego**, **USA**, July 2008.